Electronic Supplementary Material (ESI) for Chemical Science.

Supporting Information

Crystalline Nanosheets of Three-Dimensional Supramolecular Frameworks with Uniform Thickness and High Stability

Xinxin Wang, Yucheng Jin, Tianyu Zheng, Ning Li, Yuesheng Han, Baoqiu Yu, Kang Wang,* Dongdong Qi,* Tianyu Wang,* Jianzhuang Jiang*

Beijing Advanced Innovation Center for Materials Genome Engineering, Beijing Key Laboratory for Science and Application of Functional Molecular and Crystalline Materials, Department of Chemistry and Chemical Engineering, School of Chemistry and Biological Engineering, University of Science and Technology Beijing, Beijing 100083, China
*Corresponding Author(s): kangwang@ustb.edu.cn (K.W.), qdd@ustb.edu.cn (D.Q.); twang@ustb.edu.cn (T.W.); jianzhuang@ustb.edu.cn (J.J.)

I. Experimental Section.

Materials and Methods. All chemicals were used as purchased without further purification unless otherwise specified. Q[8] were prepared and purified according to the method developed in our laboratory. Q[8]/H_2PtCl_6, and Q[8]/$HAuCl_4$ were prepared according to the published procedures.[1,2]

Characterizations. Powder X-ray diffraction (PXRD) patterns were collected at room temperature on a PANalytical Empyrean series 3 diffractometer equipped with Cu Kα radiation operating at 45 kV and 40 mA, on a diffracted-beam graphite monochromator. Al Kα X-ray (6 mA × 12 KV) was utilized as the irradiation source. All measurements were performed in the CAE mode with the reference of C 1s (284.8 eV). FT-IR spectra were recorded from KBr pellets samples, using a Bruker Tensor 37 spectrometer with 2 cm^{-1} resolution. TEM images were obtained with a JEM-2100, JEOL. Energy dispersive spectroscopy (EDS) mapping images were collected by transmission electron microscopy (JEM-2100F) at an operation voltage of 200 kV. Scanning electron microscopy (SEM) images were performed on a HITACHI SU8010 microscope operated at an accelerating voltage of 10.0 KV. HR-TEM, HAADF-STEM and EDS mapping images were taken on a JEM-ARM200F electron microscope operated at 200 kV. X-ray photoelectron spectra (XPS) were collected from PHI 5300 ESCA System (PerkineElmer, USA). TG-DSC (NETZSCH STA 409 PC/PG) was applied to trace the weight loss in the carbonization stage. CV and LSV measurements were conducted on the CHI 760E workstation (CH Instruments, Inc.) with a RRDE-3A rotator (ALS Co., Ltd). The XAFS spectra at Ni K-edge were acquired at 4B9A station in Beijing Synchrotron Radiation Facility (BSRF, operated at 2.5 GeV with a maximum current of 250 mA). The raw EXAFS data acquired were then background-subtracted, normalized, and Fourier-transformed by

using the ATHENA program in the IFEFFIT software package. Least-squares curve parameter fitting was performed using the ARTEMIS module of IFEFFIT software packages. Small-angle X-ray scattering (SAXS) patterns were recorded using a 2D Pilatus detectors with the pixel size of 172 μm at beamline 1W2A of Beijing Synchrotron Radiation Facility (BSRF). The incident X-ray wavelength was fixed at 1.54 Å by a triangle bending Si(111) monochromator. The distance from the sample to detector was fixed at 1605 mm, which was calibrated by the silver behenate standard sample.

Synthesis of Q[8]/H_2PtCl_6. Q[8] (10.0 mg, 0.007 mmol) and H_2PtCl_6 (1.5 mg, 0.014 mmol) were dissolved in 6.0 M HCl (3.0 mL) *(1)*. The solutions were left to stand, allowing the volatiles to slowly evaporate in air at room temperature. Light-orange crystals were obtained from the solution within a few days. Then the precipitate was collected, washed three times with 6.0 M HCl (1.0 mL), dried in air (22.4 mg, 80%).

Synthesis of Q[8]/Pt. Q[8]/H_2PtCl_6 (106.0 g) dispersed in CH_3OH (30.0 mL) and heated at 65 ºC with stirring for 5 h. The reaction product was filtered and rinsed with water to give rise to gray solid (101.0 mg, 95%).

Synthesis of Q[8]/Pt NSs. Q[8]/H_2PtCl_6 (106.0 mg) dispersed in water (30.0 mL) and then dropped 0.020 mL 80% $N_2H_4 \cdot H_2O$ in the suspension liquid, the solution was heated at 50 ºC with stirring for 1 h. The reaction product was filtered and rinsed with water to give rise to gray black solid (98 mg, 91%).

Synthesis of Q[8]/Pt NSs films. The Q[8]/Pt NSs films were obtained through filtering a certain amount (10/20/30/40 mg) of Q[8]/Pt NSs suspension in ethanol on the filter membrane. Before catalytic test, the Q[8]/Pt NSs films were dried at 100 ºC for 12 h in the vacuum oven.

Preparation of Q[8]/Pt films. 20 mg of the Q[8]/Pt was dispersed in ethanol and then uniformly coated on a round glass plane (the diameter is 35 mm). Before catalytic test, the glass plane coated with Q[8]/Pt film was dried at 100℃ for 12 h in the vacuum oven.

Photocatalytic stability of Q[8]/Pt NSs films. Five runs of consecutive photocatalytic CO oxidation were carried out to evaluate the cyclability and stability of Q[8]/Pt NSs films. In detail, after each cycle, gas replacement of idealized gas mixture 0.8% CO, 20% O_2, and He balance in the reactor was performed to remove air and then for the sequential run for photocatalytic CO oxidation by the procedure detailed above. The post characterization of catalyst was conducted using the following sample processing method: after the photocatalytic CO oxidation reaction completed, the sample was scraped from the films and collected to perform structural characterization.

Photocatalytic CO oxidation. The prepared films were placed on a glass bracket in a 150 mL photocatalytic reactor. Gas replacement in the reactor was performed to remove air, ensuring that the final reactor was filled with an idealized gas mixture 0.8% CO, 20% O_2, and He balance. A 300 W xenon lamp with a cut filter (to ensure effective wavelengths are in the range of 400 to 800 nm) was used as light source. After a certain period of irradiation, 0.5 mL of the gas sample was taken and subjected to gas chromatography (GC 7920) to measure the amounts of CO_2.

Thermocatalytic CO oxidation. The catalytic performance of Q[8]/Pt NSs films oxidation was evaluated in a flow reactor. The feed gas was composed of 0.8% CO, 20% O_2, and He balance, which passed through the reactor at a flow rate of 25 ml min-1. The effluent gas compositions were analysed online by a gas chromatograph (GC 7920). We examined the temperature-dependent catalytic activity of Q[8]/Pt NSs films between 25

and 150 °C using appropriate amounts of catalyst at each temperature.

Computational Details. Density functional theory (DFT) calculations were carried out at the level of PBE-GrimmeD3/DND3.5(effective core potential) level[3] using the Nøskov mode[4,5] in the DMol3 software.[6]

The interaction between molecular building blocks in Q[8]/H_2PtCl_6 and Q[8] single crystals.

The exact interactions as well as intensity existing among the molecular building blocks in both Q[8]/H_2PtCl_6 and Q[8] single crystals are clarified at the level of M06/SDD/6-311+G(d). As shown in Figure S22, each Q[8] molecule is fixed by six Q[8] and two H_2PtCl_6 molecules in the Q[8]/H_2PtCl_6 crystal. The stabilization energy (E_S) of the target Q[8] molecule (**T** in Figure S9) could be calculated in the following manner:

$$\Delta E_S = \frac{1}{2}\times(4E_{T-A} + 2E_{T-B} + 2E_{T-C})$$
$$= \frac{1}{2}\times[4\times(-108\text{kJ/mol}) + 2\times(-16\text{kJ/mol}) + 2\times(-34\text{kJ/mol})]$$
$$= -266\text{kJ/mol}$$

But in the Q[8] crystal, the H_2PtCl_6 molecule is removed. Now each Q[8] molecule is fixed by six Q[8] molecules. The stabilization energy (E_S) of the target Q[8] molecule could be calculated in the following manner:

$$\Delta E_S = \frac{1}{2}\times(4E_{T-A} + 2E_{T-B})$$
$$= \frac{1}{2}\times[4\times(-112\text{kJ/mol}) + 2\times(-17\text{kJ/mol})]$$
$$= -241\text{kJ/mol}$$

Formation Mechanism of the crystalline nanosheets of Q[8]/Pt NSs. It is worth noting that the existing state of hydrazine hydrate is not as simple as the stoichiometric formula of $N_2H_4{\cdot}H_2O$. Due to the multiple N···H/O···H bonds, Figure S23, a few $N_2H_4{\cdot}H_2O$

molecules could be linked together to form an oligomeric $(N_2H_4{\cdot}H_2O)_n$ chain in solution. As a consequence, when the third $N_2H_4{\cdot}H_2O$ molecule gets into this channel, it will be followed by other $N_2H_4{\cdot}H_2O$ molecules as a curved chain. Once the $N_2H_4{\cdot}H_2O$ molecule touches the H_2PtCl_6 molecule embedded between the sixth and seventh Q[8] layers in the single crystal, the repeated explosion certainly occurs again. However, the gas releasing pathway is blocked by other $N_2H_4{\cdot}H_2O$ molecules in the curved channel at the present stage. The gases yielded then find no way to go but become a power to push away the “wall” yielded thus far, the thin nanosheets of 3D SMF constructed by six Q[8] layers with a thickness of ca. 4.8 nm, under the help of heat yielded simultaneously. It is noteworthy that according to the single crystal X-ray diffraction analysis result of Q[8], the thickness of six Q[8] layers along *b* direction in single crystal just amounts to 4.8 nm. Driven by such kind of microscopic explosion, the nanosheets of 3D SMF fall off from the bulk Q[8]/H_2PtCl_6 single crystal to enter the solution system and gets contacted with more $N_2H_4{\cdot}H_2O$ molecules in the water solution. After the formation of nanosheet of 3D SMF, the newly-generated Pt atoms will also assemble into more Pt nanocrystals. When all the Pt nanocrystals are immobilized at the surface of Q[8] nanosheets due to the interaction of (Pt nanocrystal)-Pt…O=C-(Q[8]), electron transfer from Pt nanocrystals to Q[8] molecules occurs. This in turn becomes responsible for the observation of the Pt^{2+} signal in the XPS and XAS spectra of Q[8]/Pt NSs. Till now, the crystalline ultrathin nanosheet of 3D SMF with Pt nano-crystals immobilized on the surface is finally fabricated and separated away from the bulk Q[8]/H_2PtCl_6 single crystal. Now, the new solid-liquid reaction interface of bulk Q[8]/H_2PtCl_6 single crystal is exposed, waiting for the next reducing process in a repeated manner.

When we look back to the full $Pt^{IV} \rightarrow Pt^0$ reduction process, we could find out a total exploring reaction depicted by *Eq. 1*. With the help of a large amount of heat (Δ_rH_m = -127 kJ/mol) yielded according to the above-described equation, 7 mol gases (N_2 and HCl) per mol reaction push the nanosheets "wall" with six Q[8] layers and *ca*. 4.8 nm thickness away from the bulk Q[8]/H_2PtCl_6 single crystal. Obviously, the curved channel with small cavity size in Q[8]/H_2PtCl_6 single crystal plays important role in promoting the gas- and heat-releasing explosive effect for yielding the crystalline nanosheets of Q[8] SMF with uniform thickness.

The catalytic mechanism of CO→CO_2. According to the calculation results, the detailed catalytic mechanism of CO→CO_2 could be divided into three steps including (1) the formation of reacting combination, (2) the O_2 activiation and first CO_2 generation, and (3) the second CO_2 gerneration.

The Pt nanocrystals (**1**) firstly adsorb the CO molecules and construct the *CO (**2**) combination with the adsorption heat decrease of 0.93 eV, Figure S40. If the O_2 molecules are linked to the Pt atoms adjacent to *CO (**2**), a new *O_2-*CO combination (**3**) will be constructed in the reaction system. It is worth noting that in this step the electronic structure of O_2 molecule is transferred from the triplet state as the independent molecule to the singlet state in **3**.

$$\mathbf{1} + CO \rightarrow \mathbf{2}, (\Delta_rG_m = -0.93\ eV)$$

$$\mathbf{2} + O_2 \rightarrow \mathbf{3}, (\Delta_rG_m = -2.54\ eV)$$

Driven by the energy input in the manner of visible light irradiation or thermal vibration at ca. 80 °C, the O-O bond could be activated along with the formation of the transition state [*O···O···*C=O] with the potential barrier of 1.15 eV. This transition state

then gets split into O* and CO_2 with a significant Gibbs free energy decrease as high as 2.48 eV.

$$\mathbf{3} \rightarrow [*O\cdots O\cdots *C{=}O]^{\neq} \rightarrow \mathbf{4},\ (\Delta_r G_{m(\mathbf{3}\rightarrow\neq)} = +1.15\ \text{eV},\ \Delta_r G_{m(\neq\rightarrow\mathbf{3})} = -2.48\ \text{eV})$$

The newly-generated CO_2 will leave from the Pt catalytic site, which will be immeditaly re-occupied by another CO molecule with the adsorption energy of 0.96 eV. This CO molecule will be further oxidized into CO_2 by the O* with the energy decrease of 1.02 eV. Finally, **6** releases the second CO_2 molecule and return to the initial state (**1**), completing one catalytic cycle.

$$\mathbf{4} + CO \rightarrow CO_2 + \mathbf{5},\ (\Delta_r G_m = -0.96\ \text{eV})$$

$$\mathbf{5} \rightarrow \mathbf{6},\ (\Delta_r G_m = -1.02\ \text{eV})$$

$$\mathbf{6} \rightarrow CO_2 + \mathbf{1},\ (\Delta_r G_m = 0.44\ \text{eV})$$

DFT calculation results of C-O stretching vibrations. As shown in Fig. S48, the simulated C-O stretching vibration in the Pt-CO model and the free CO_2 molecule is 2060 and 2328 cm^{-1}, respectively. This result indicate that the peaks at *ca*. 2060-2064 cm^{-1} observed in the *in situ* DRIFTS measurements is due to the adsorption of CO on Pt nanoparticles in Q[8]/Pt NSs, further confirming the CO-to-CO_2 conversion under the catalysis of Q[8]/Pt NSs.

II. Characterizations and Properties.

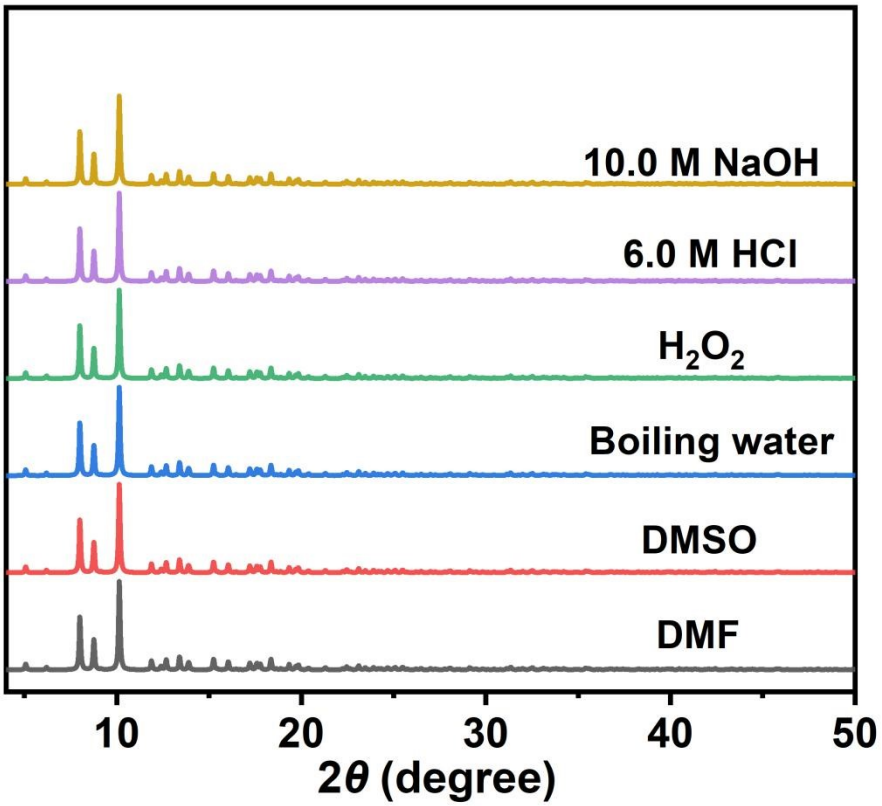

Fig. S1. PXRD patterns for Q[8] single crystals after various treatments for 24 h.

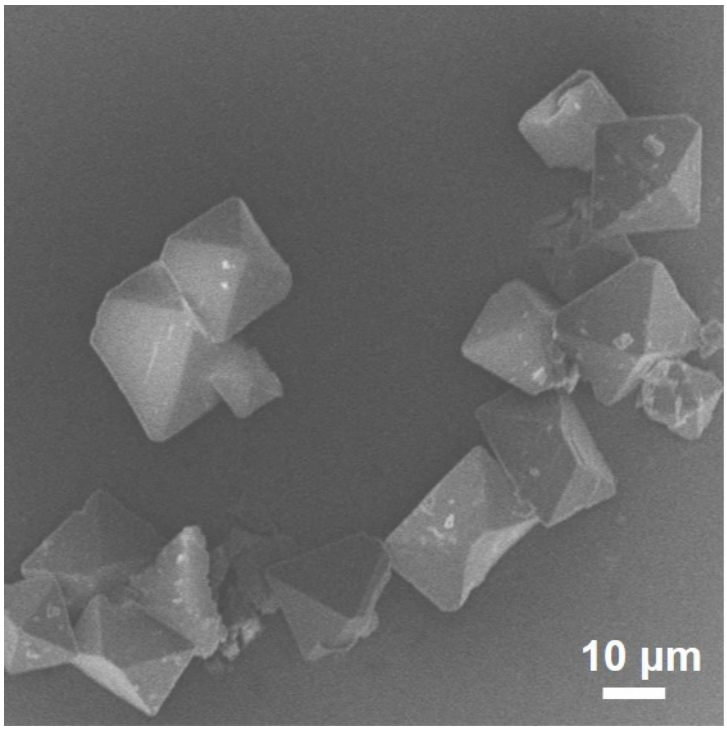

Fig. S2. SEM image of block-shaped Q[8] single crystals after sonication in ethanol for 12 h.

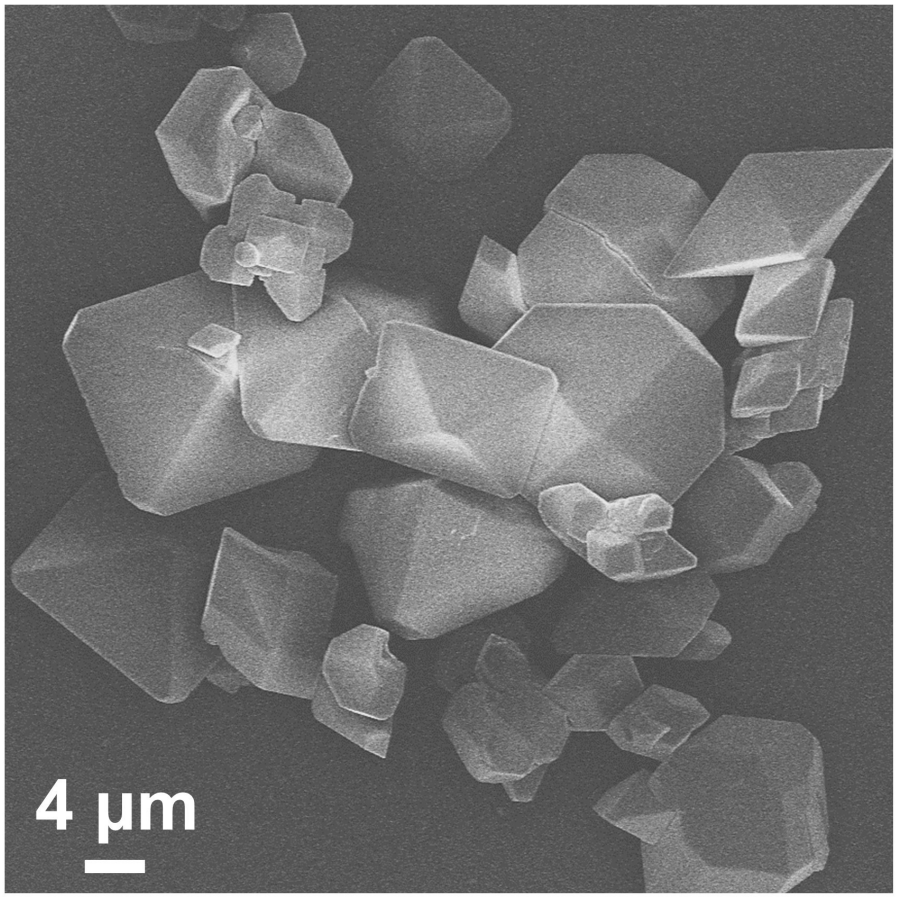

Fig. S3. SEM image of block-shaped Q[8]/H_2PtCl_6 single crystals after sonication in ethanol for 5 min.

Fig. S4. SEM image of square-like Q[8]/Pt NSs after sonication in ethanol for 5 min.

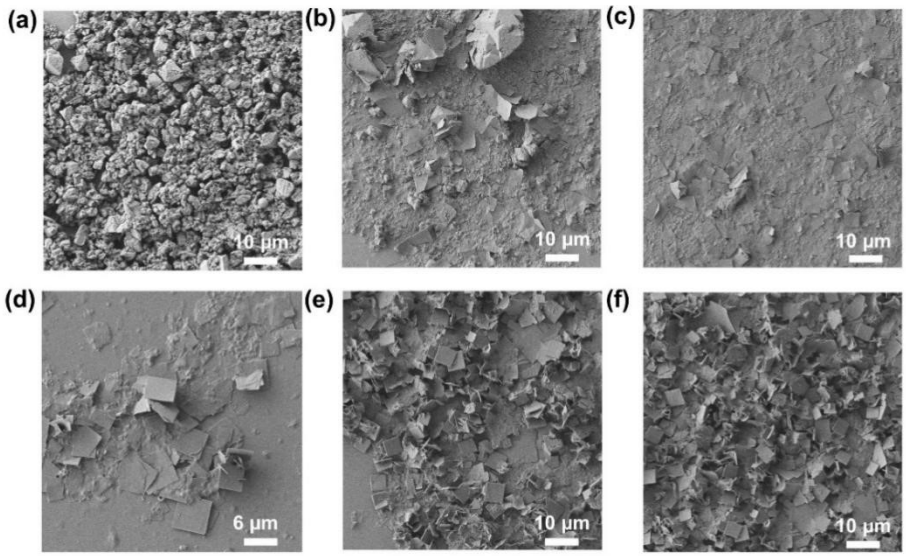

Fig. S5. SEM images of Q[8]/Pt NSs collected at different reaction times in HH: (a) 10 s, (b) 10 min, (c)30 min, (d) 60 min, (e) 90 min and (f) 120 min.

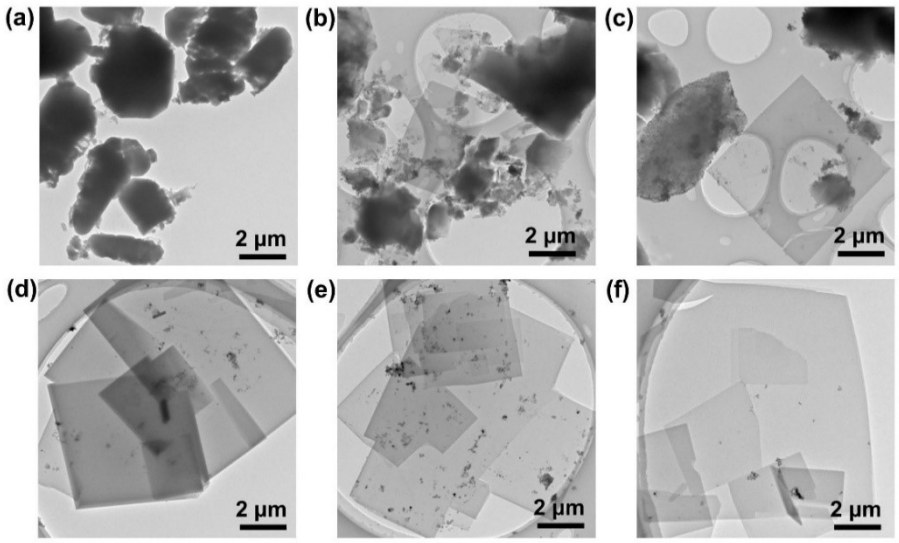

Fig. S6. TEM images of Q[8]/Pt NSs collected at different reaction times in HH: (a) 10 s, (b) 10 min, (c)30 min, (d) 60 min, (e) 90 min and (f) 120 min.

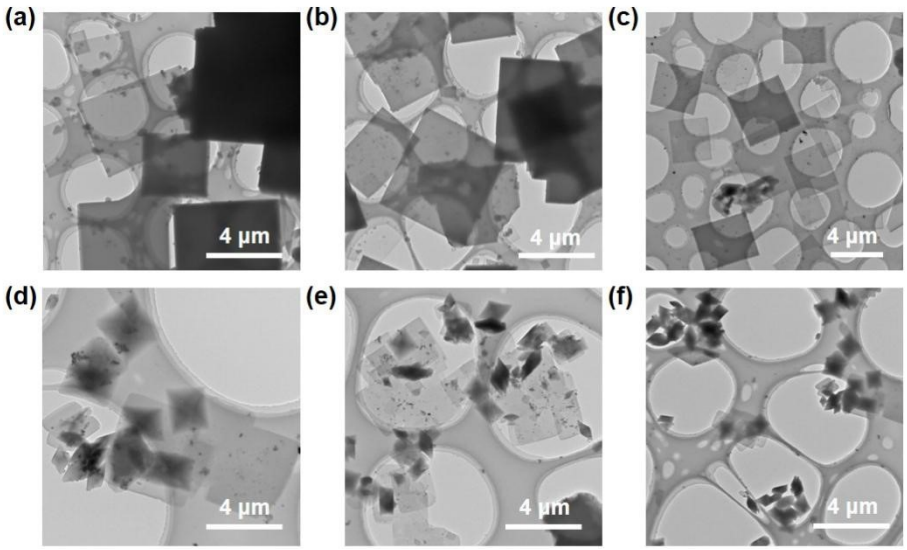

Fig. S7. TEM images of Q[8]/Pt NSs collected at different concentrations of HH: (a) 2.0 mmol/L, (b) 6.0 mmol/L, (c) 12.0 mmol/L, (d) 18.0 mmol/L, (e) 24.0 mmol/L, and (f) 30.0 mmol/L.

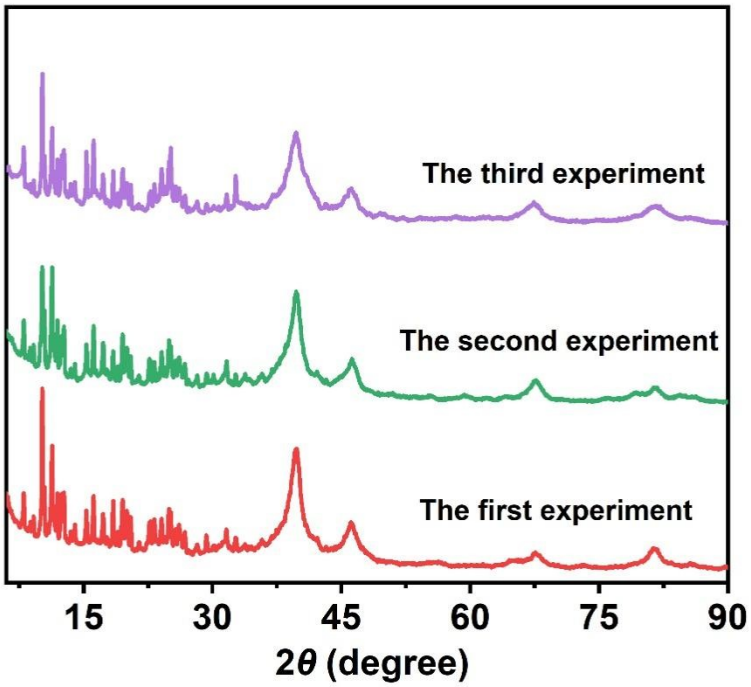

Fig. S8. PXRD patterns for Q[8]/Pt NSs.

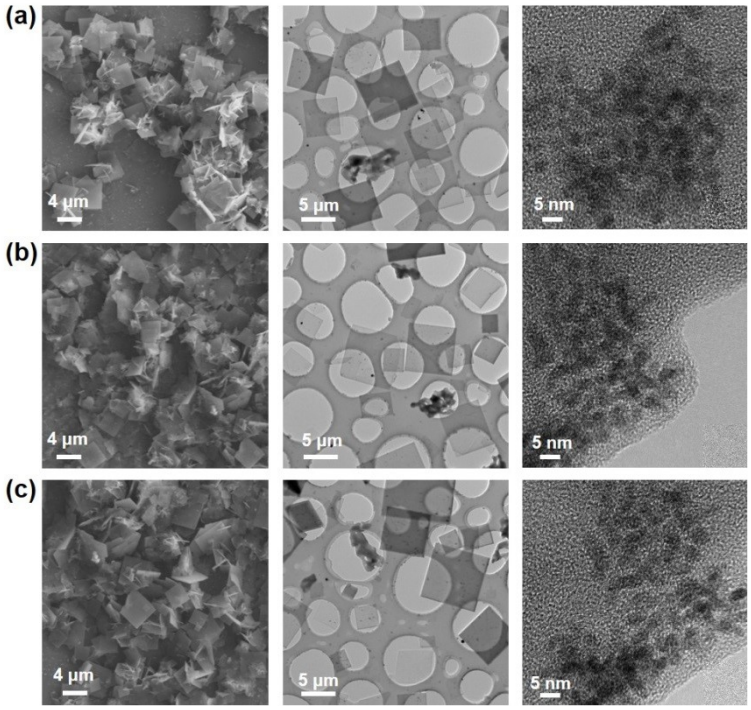

Fig. S9. Characterizations of crystalline ultrathin Q[8]/Pt NSs. (a, b, c) TEM, SEM images of Q[8]/Pt NSs and HR-TEM images of Pt nanoparticles.

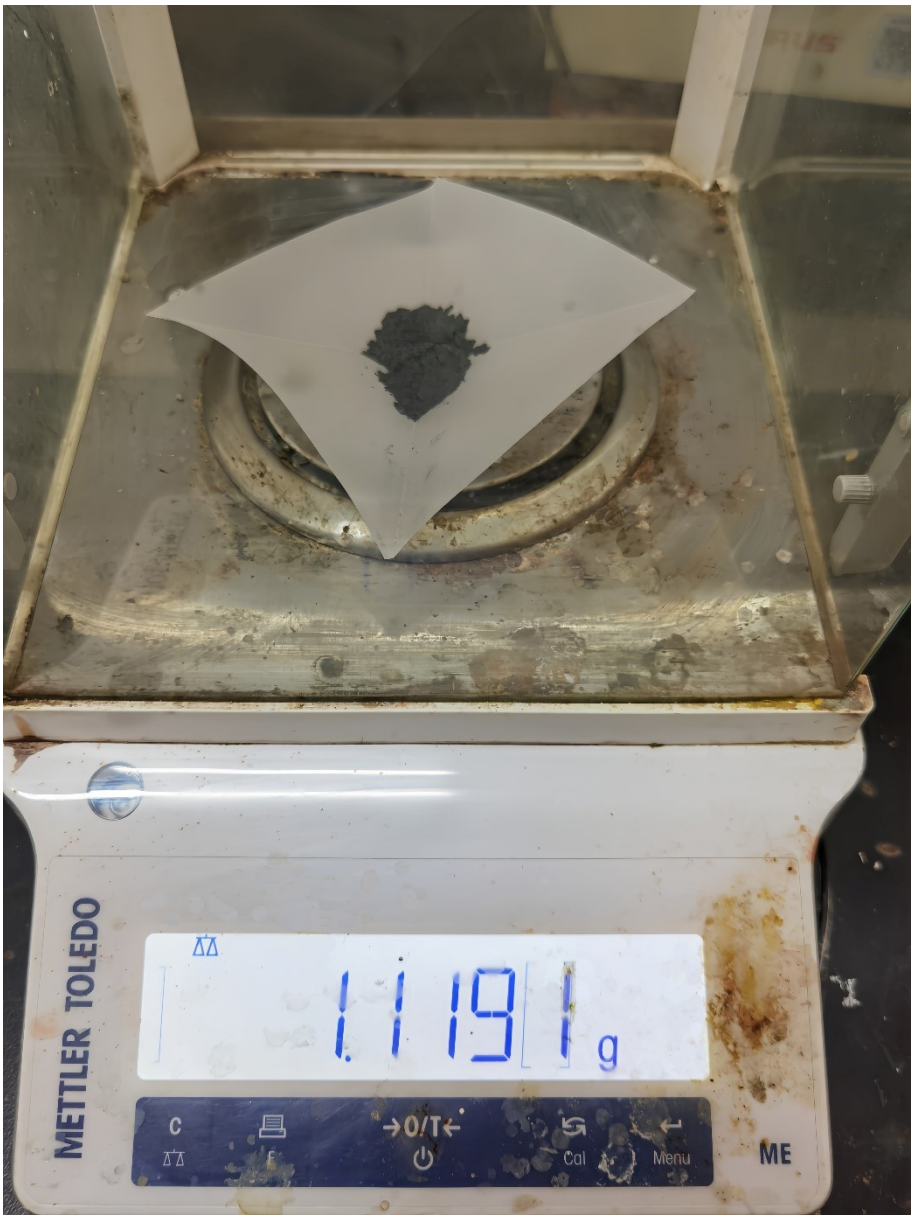

Fig. S10. Photos of the large-scale production of Q[8]/Pt NSs catalyst.

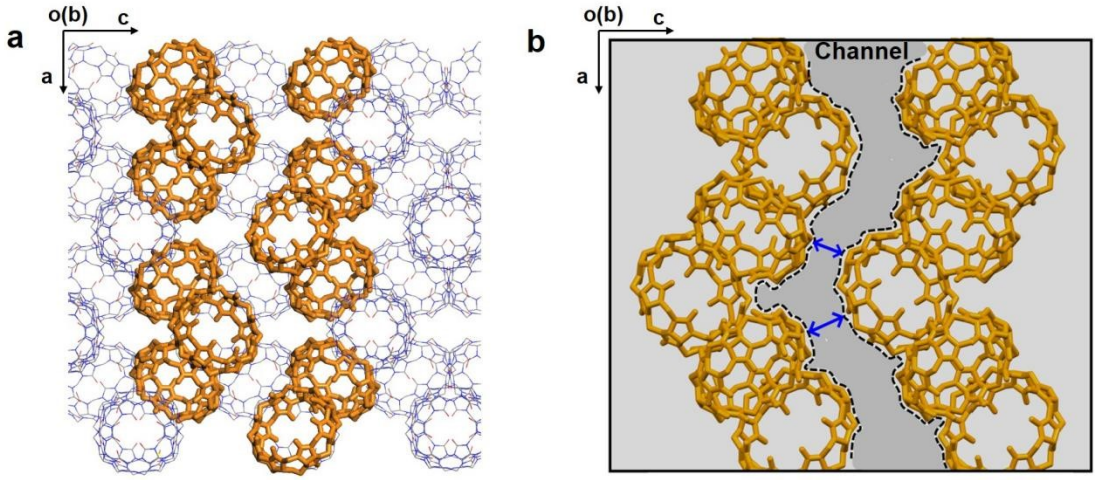

Fig. S11. (a) The crystal structure and (b) the curved channel in Q[8] crystal.

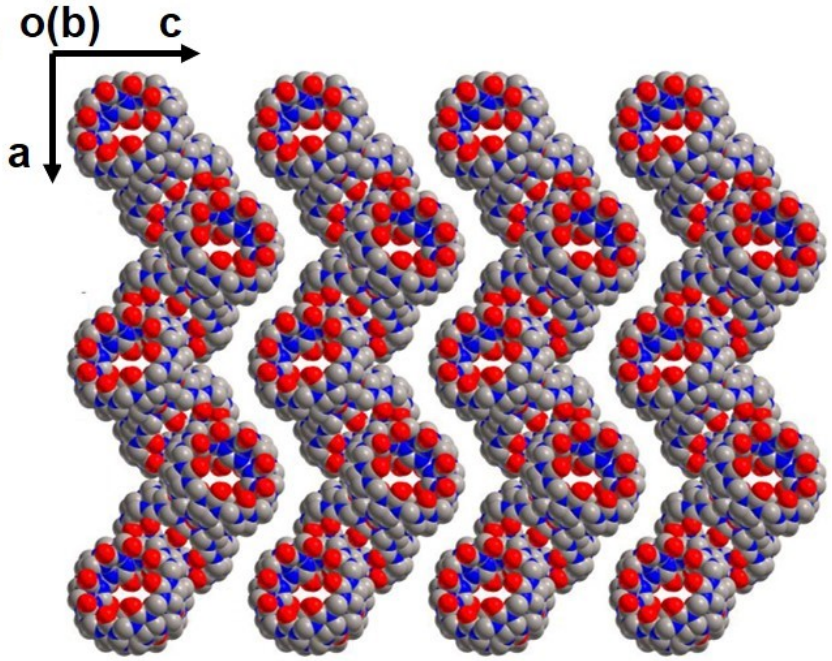

Fig. S12. The crystal structure with the curved channel in Q[8].

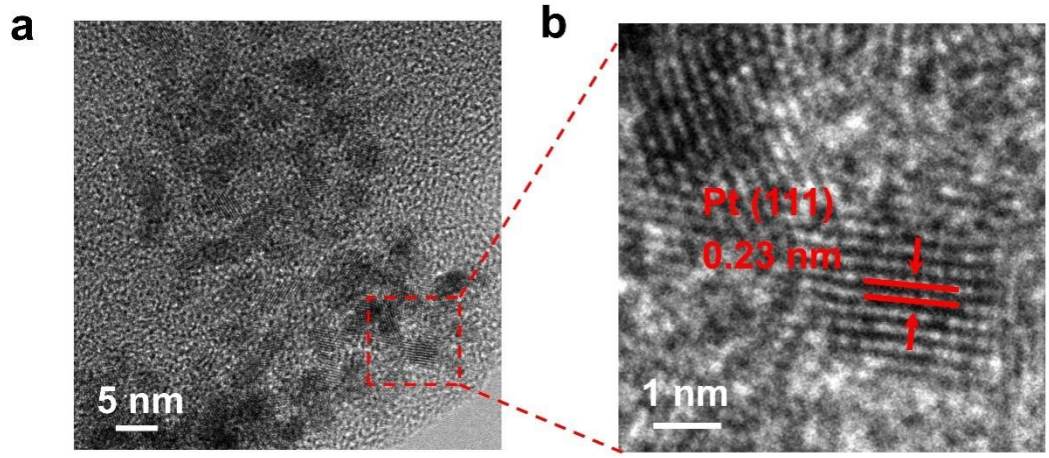

Fig. S13. (a) HR-TEM and (b) enlarged HR-TEM images of Pt nanoparticles.

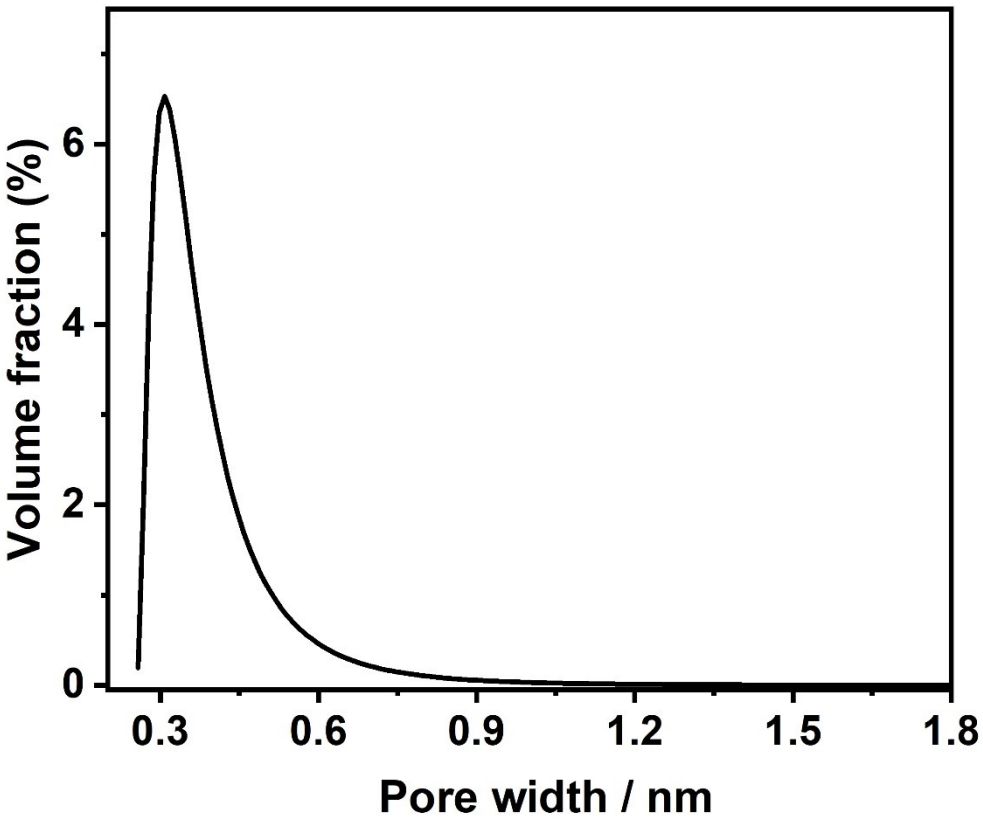

Fig. S14. Pore size distribution of Q[8]/Pt NSs calculated from SAXS data.

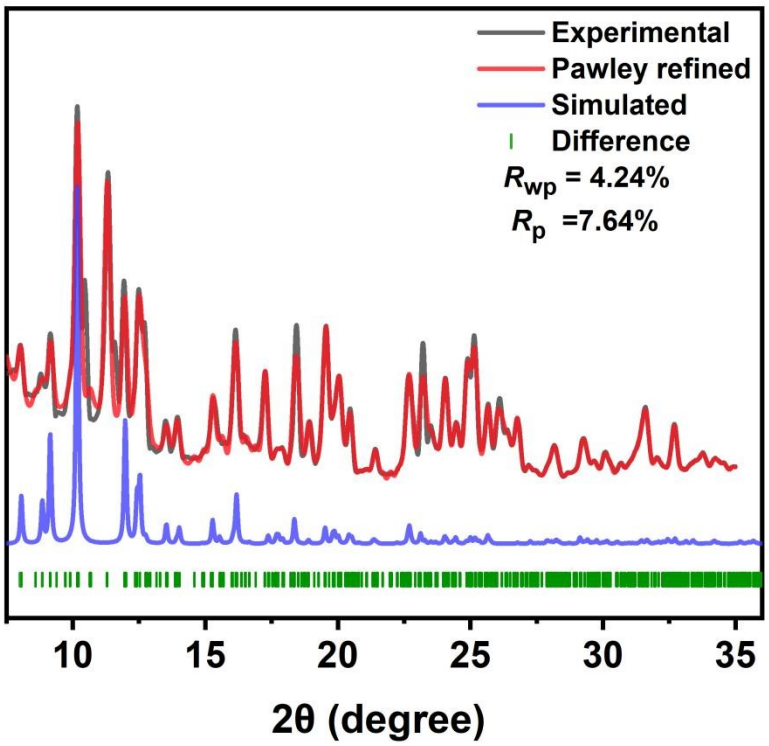

Fig. S15. Q[8]/Pt NSs experimental PXRD profile (black), refined profile (red), and simulation pattern (blue).

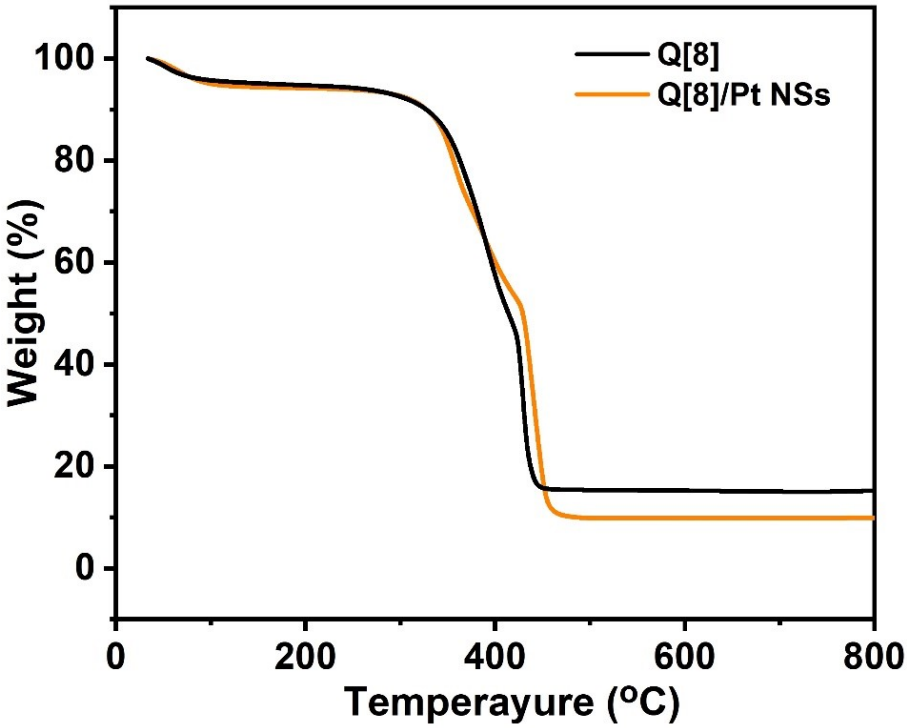

Fig. S16. TGA analysis of Q[8] and Q[8]/Pt NSs.

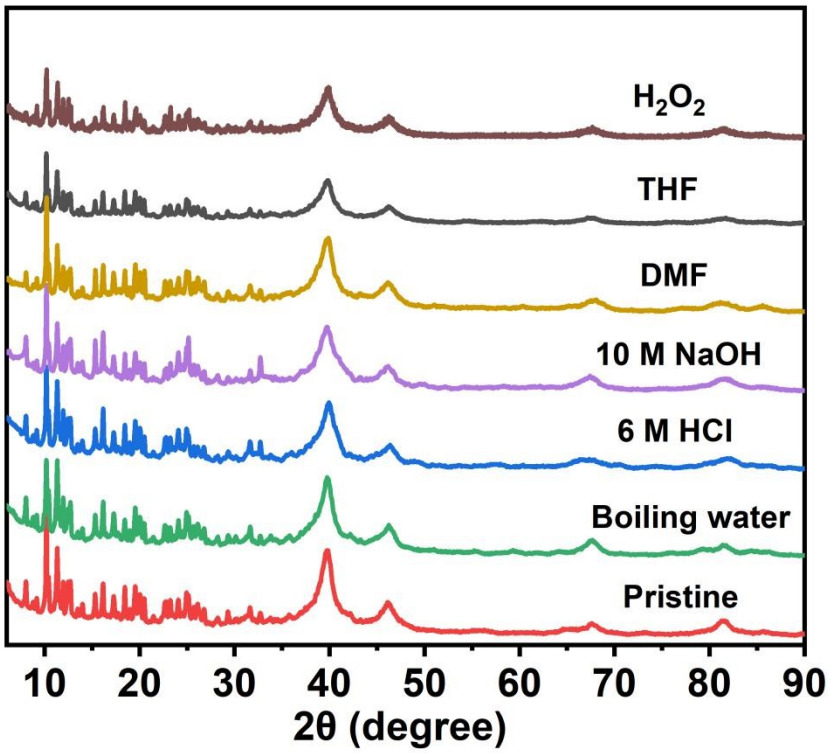

Fig. S17. PXRD patterns for Q[8]/Pt NSs after various treatments for 24 h.

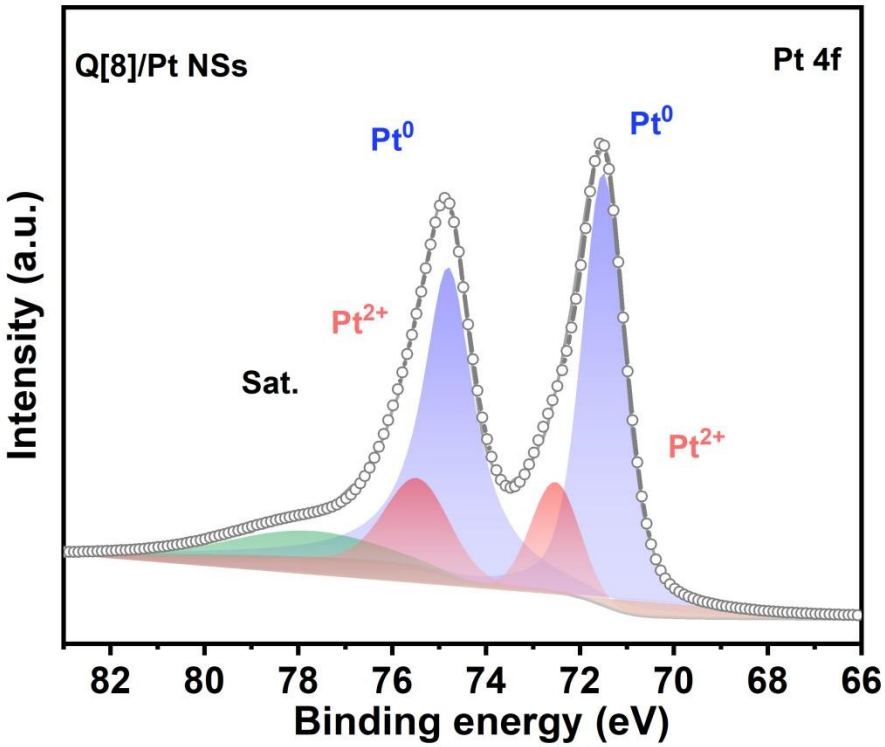

Fig. S18. High-resolution XPS spectrum of Pt 4f for Q[8]/Pt NSs.

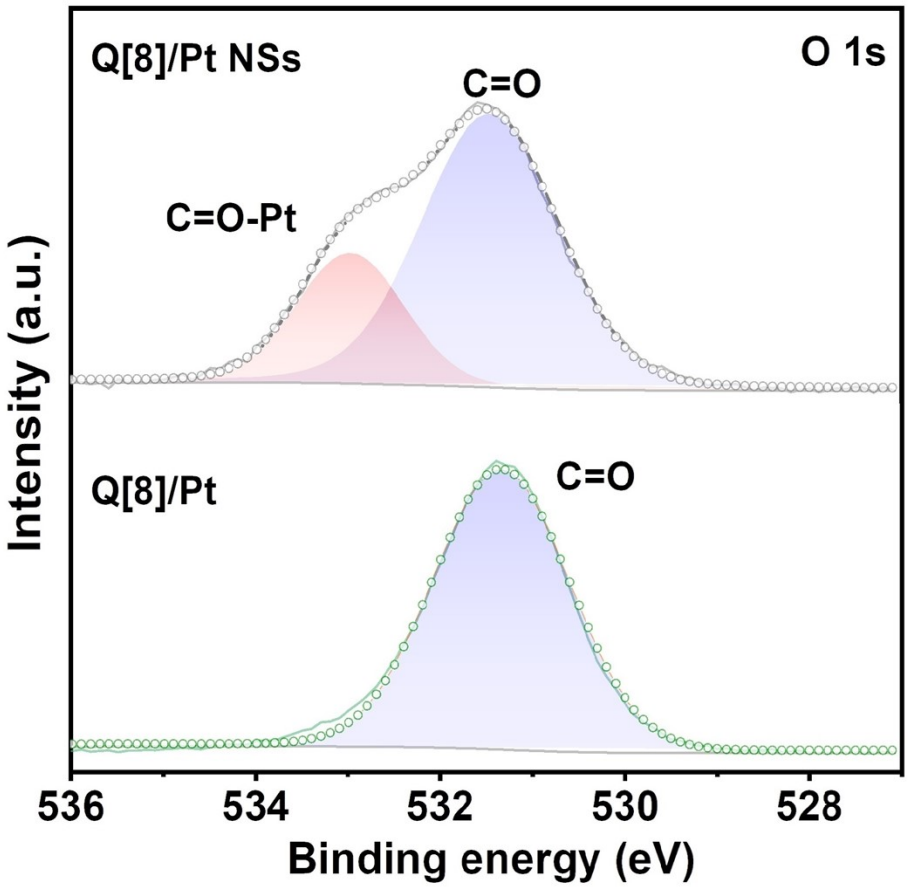

Fig. S19. The high-resolution O 1s XPS spectra of Q[8]/Pt NSs and Q[8] single crystals.

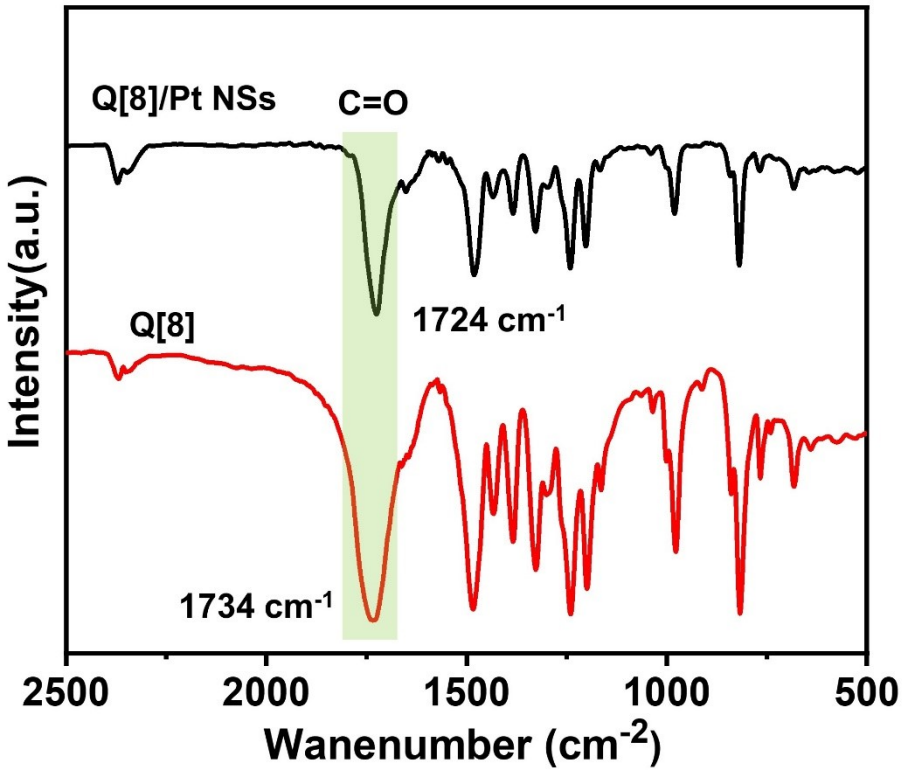

Fig. S20. FT-IR spectra of Q[8] and Q[8]/Pt NSs.

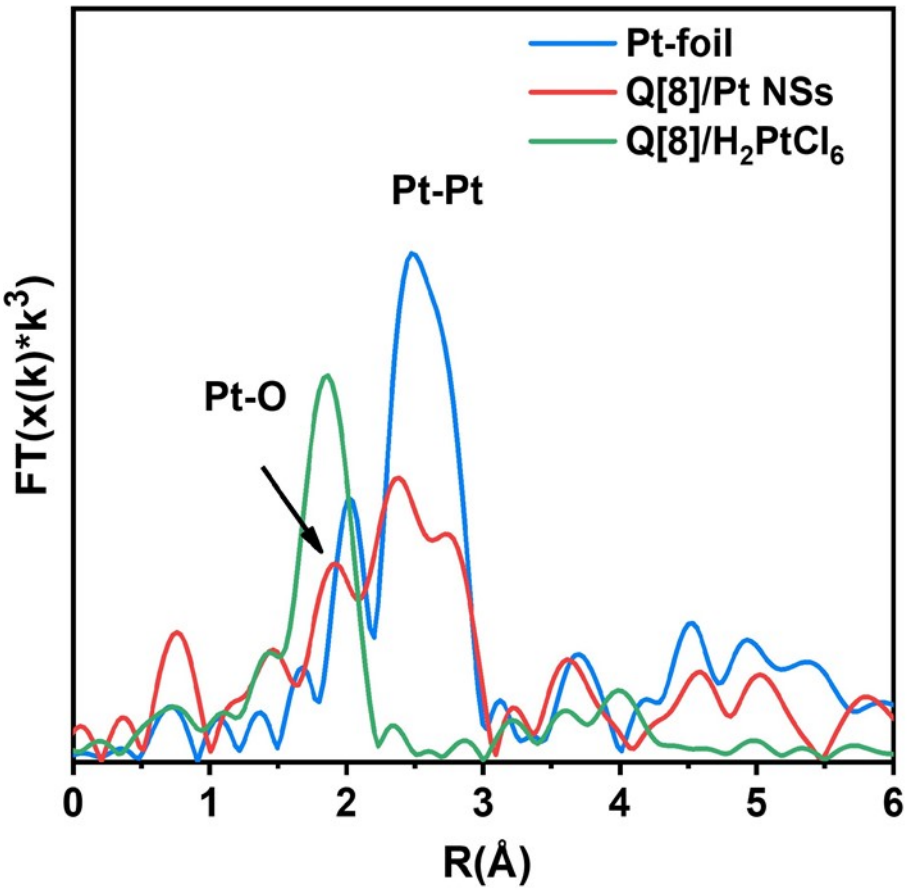

Fig. S21. XANES spectra of Q[8]/Pt NSs, Pt foil, and PtO_2.

Fig. S22. EXAFS spectra of Q[8]/Pt NSs, Pt foil, and PtO_2.

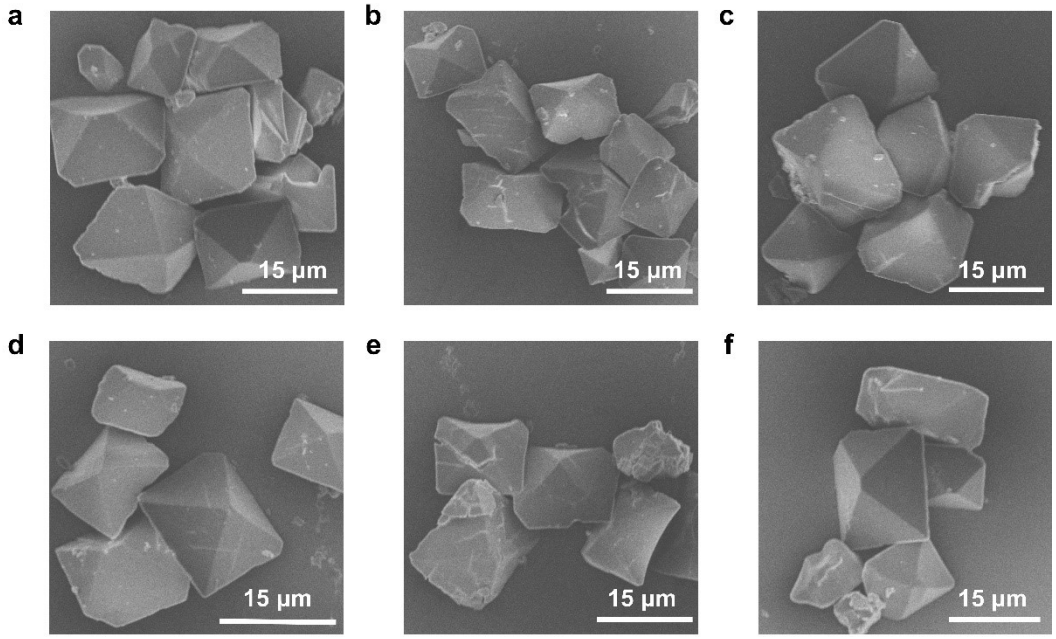

Fig. S23. SEM images of Q[8]/H_2PtCl_6 collected at different reaction times in methanol: (a) 10 min, (b) 60 min, (c) 120 min, (d) 180 min, (e) 240 min, and (f) 300 min.

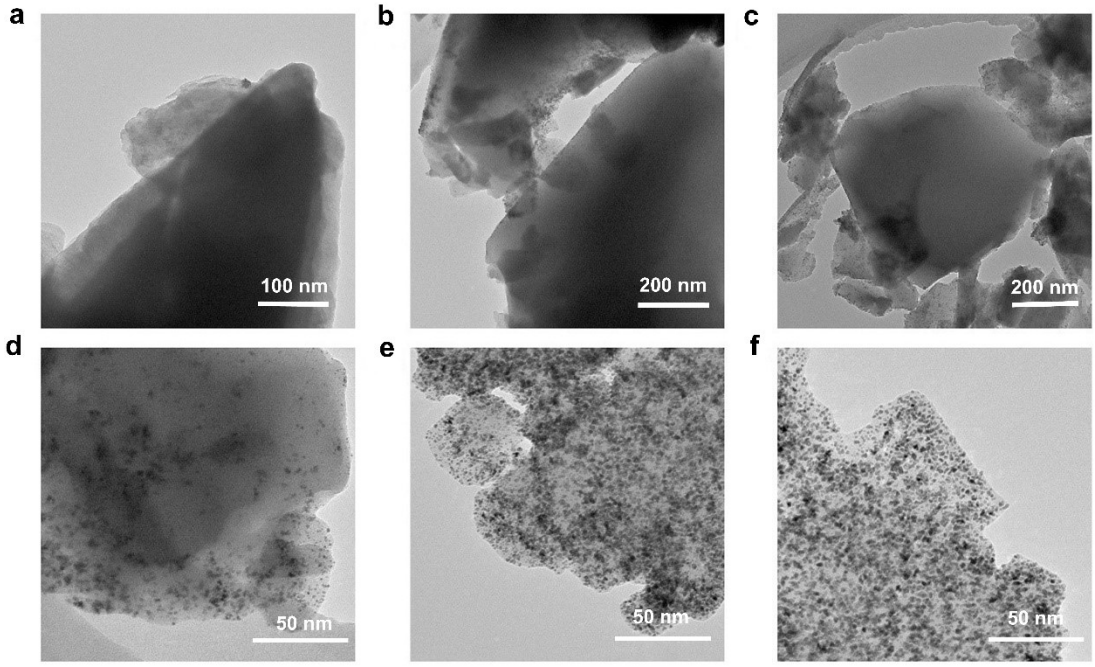

Fig. S24. TEM images of Q[8]/H_2PtCl_6 collected at different reaction times in methanol: (a) 10 min, (b) 60 min, (c) 120 min, (d) 180 min, (e) 240 min, and (f) 300 min.

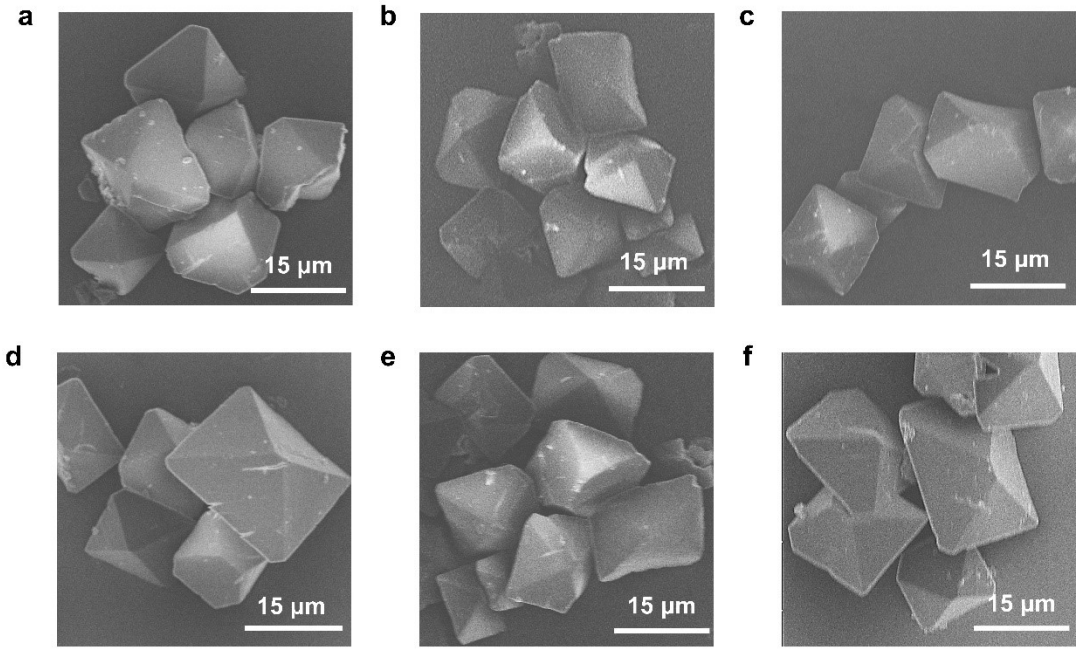

Fig. S25. SEM images of Q[8]/H_2PtCl_6 collected at different reaction times in glycol: (a) 10 min, (b) 60 min, (c) 120 min, (d) 180 min, (e) 240 min, and (f) 300 min.

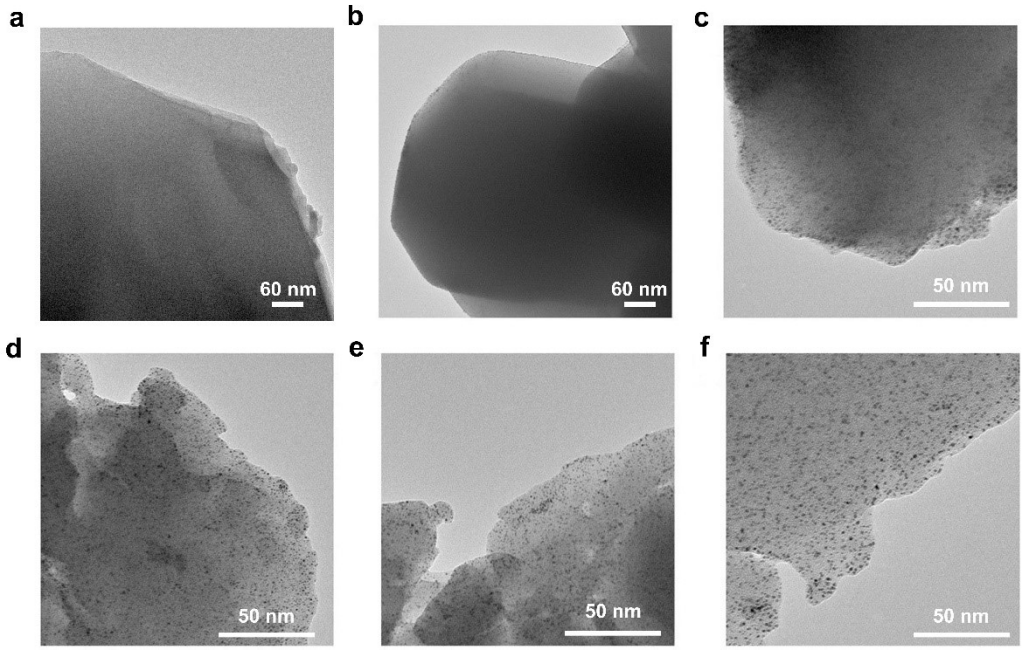

Fig. S26. TEM images of Q[8]/H_2PtCl_6 collected at different reaction times in glycol: (a) 10 min, (b) 60 min, (c) 120 min, (d) 180 min, (e) 240 min, and (f) 300 min.

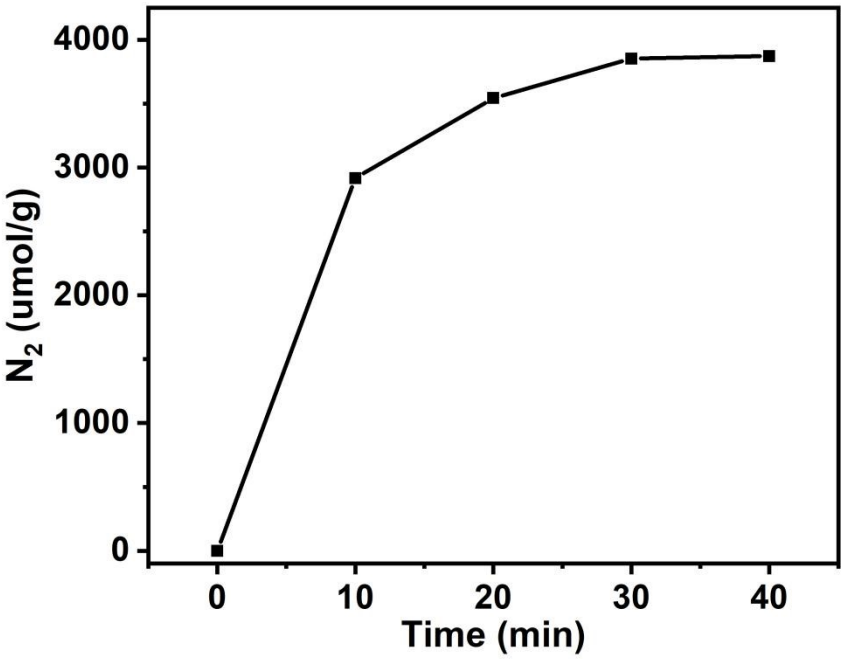

Fig. S27. Time-dependent N_2 generation profile in the reaction system of Q[8]/H_2PtCl_6 crystals and hydrazine hydrate.

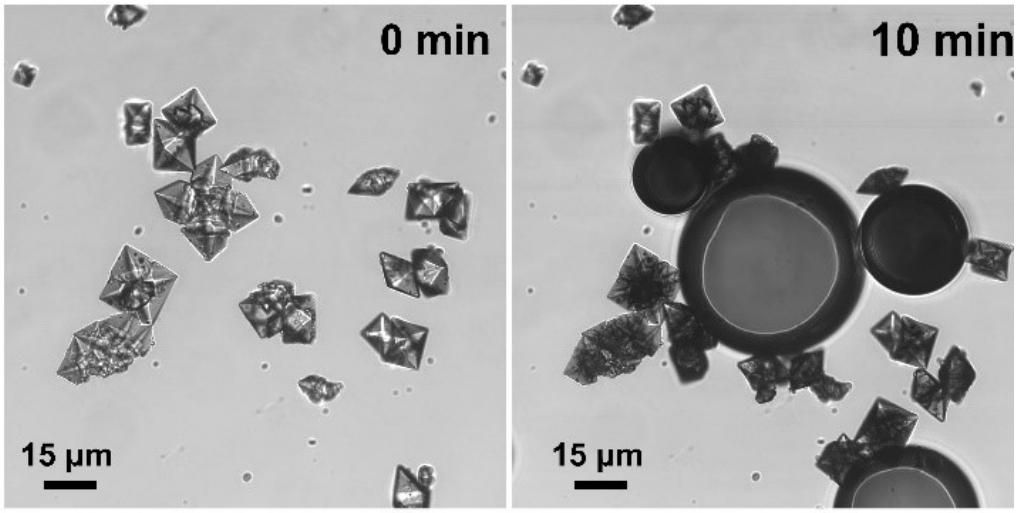

Fig. S28. Representative bright-field microscopy images of the Q[8]/H_2PtCl_6 crystals and $N_2H_4 \cdot H_2O$ reaction system at 0 min and 10 min.

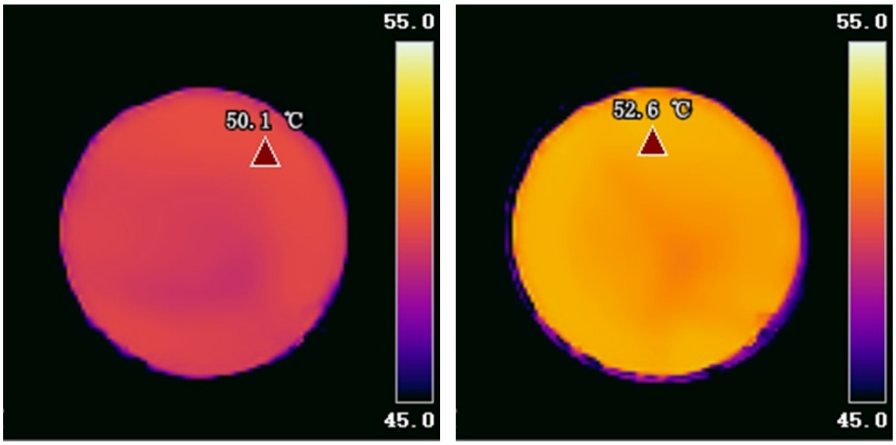

Fig. S29. The temperature comparison before (left) and after (right) reaction between 10.0 mg Q[8]/H_2PtCl_6 single crystals and 0.02 mL $N_2H_4 \cdot H_2O$ for 10 min.

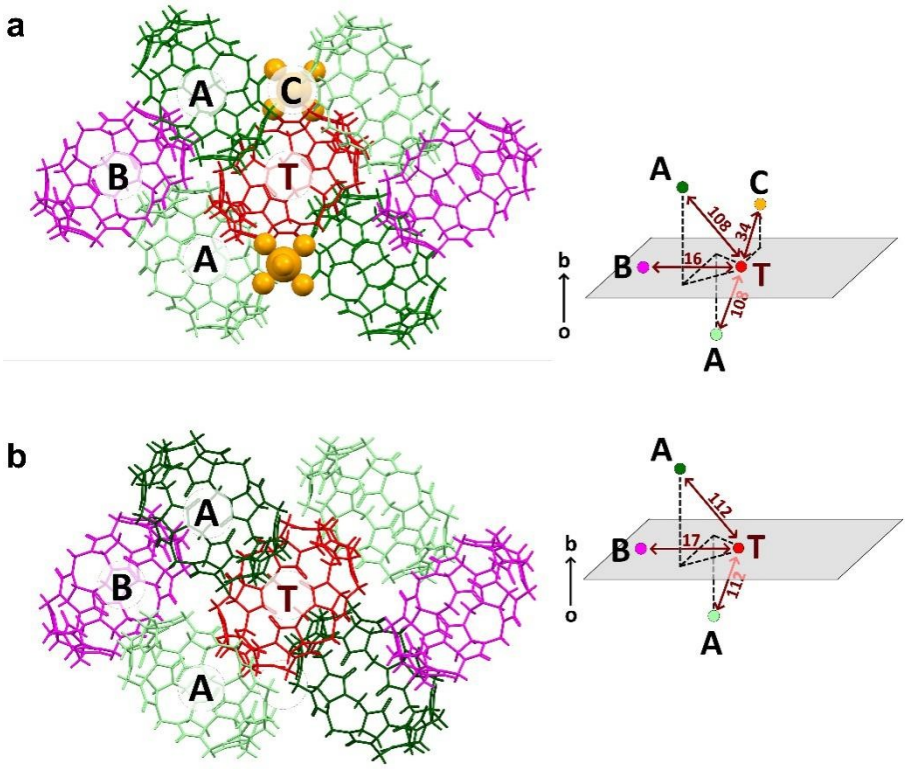

Fig. S30. The interaction between molecular building blocks in (a) Q[8]/H_2PtCl_6 and (b) Q[8] single crystals.

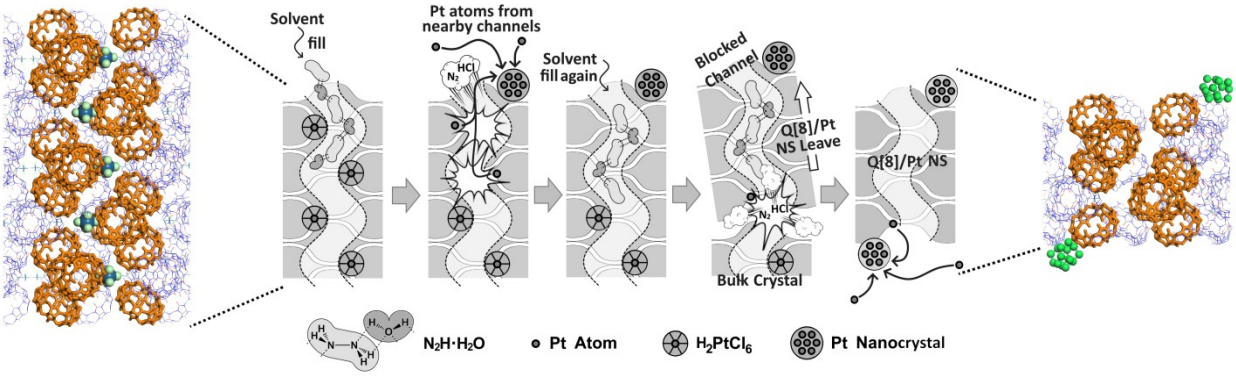

Fig. S31. The curved channel in Q[8]/H_2PtCl_6 together with the proposed formation mechanism of Q[8]/Pt NSs.

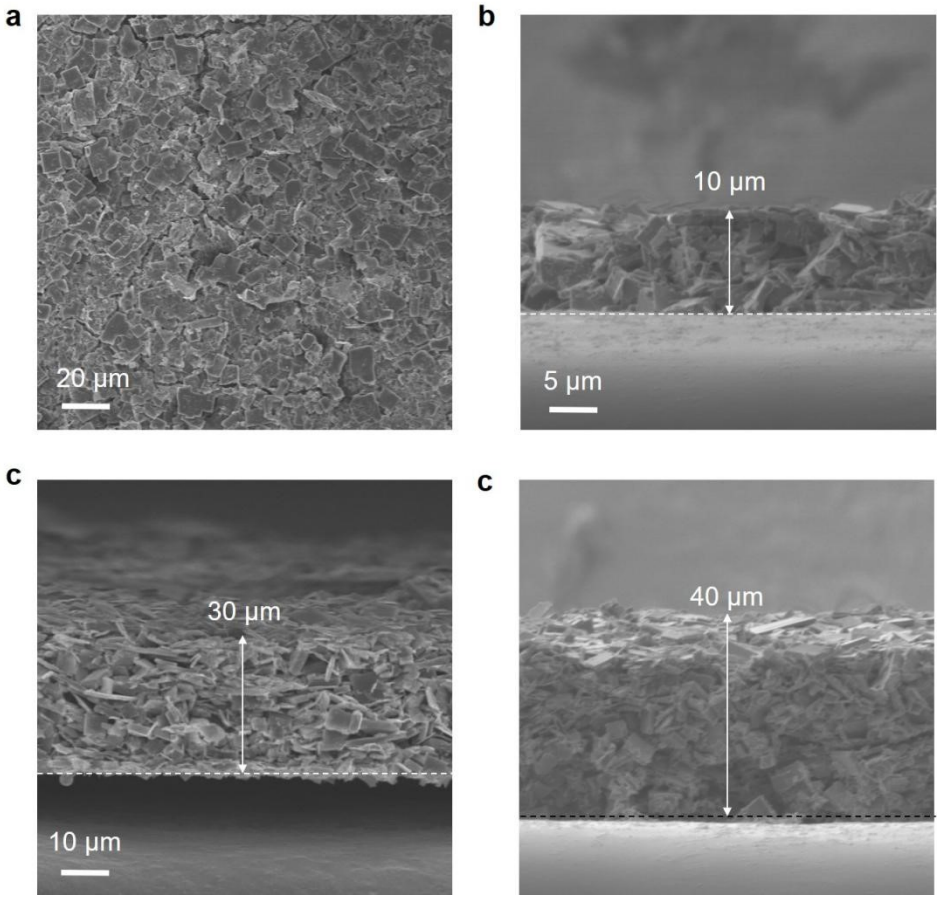

Fig. S32. (a) Surface and (b-d) cross-section morphologies of Q[8]/Pt NSs films.

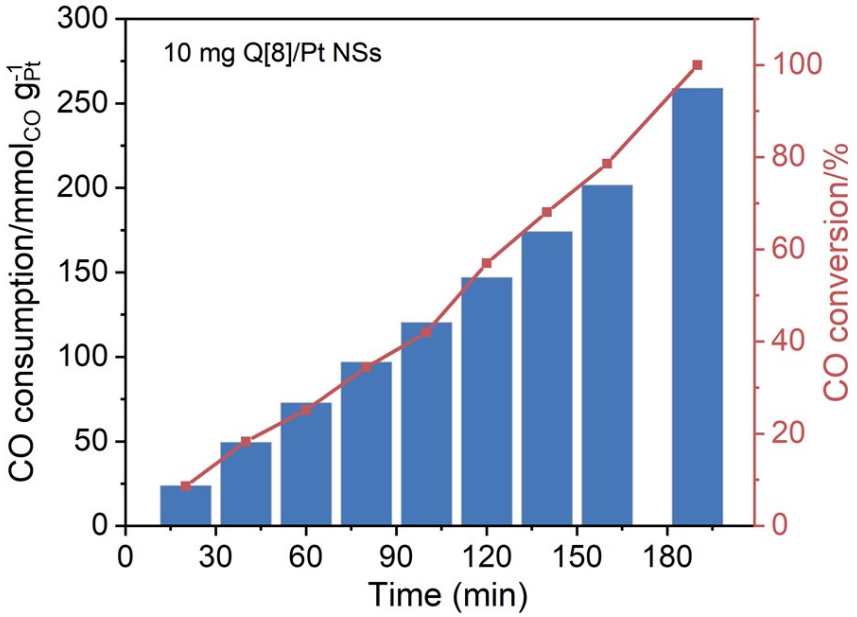

Fig. S33. Photocatalytic CO oxidation activities of Q[8]/Pt NSs film-10 at 25 °C in an idealized gas mixture (0.8% CO, 20% O_2, and He balance).

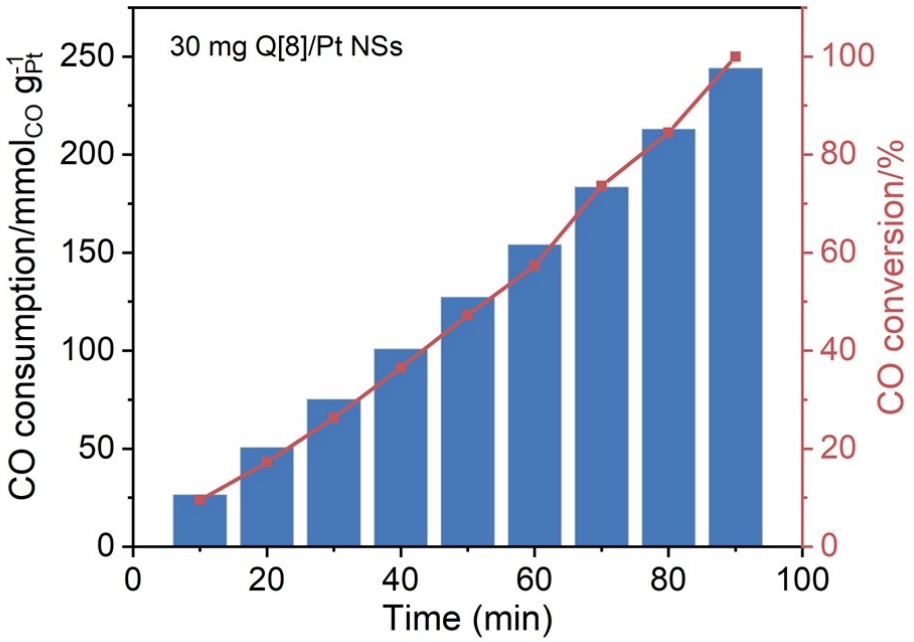

Fig. S34. Photocatalytic CO oxidation activities of Q[8]/Pt NSs film-30 at 25 °C in an idealized gas mixture (0.8% CO, 20% O_2, and He balance).

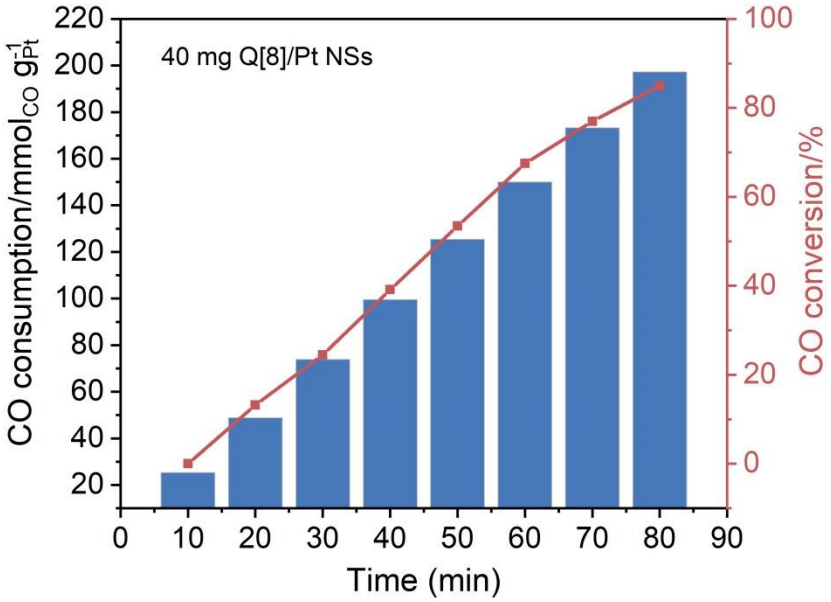

Fig. S35. Photocatalytic CO oxidation activities of Q[8]/Pt NSs film-40 at 25 °C in an idealized gas mixture (0.8% CO, 20% O_2, and He balance).

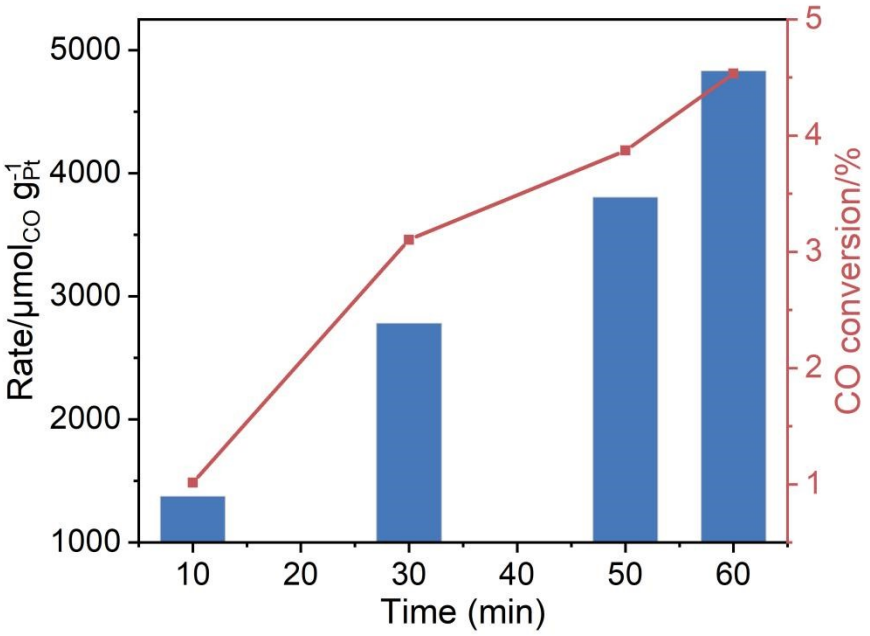

Fig. S36. Photocatalytic CO oxidation activities of the CH_3OH-reduced Q[8]/Pt film-20 in an idealized gas mixture (0.8% CO, 20% O_2, and He balance).

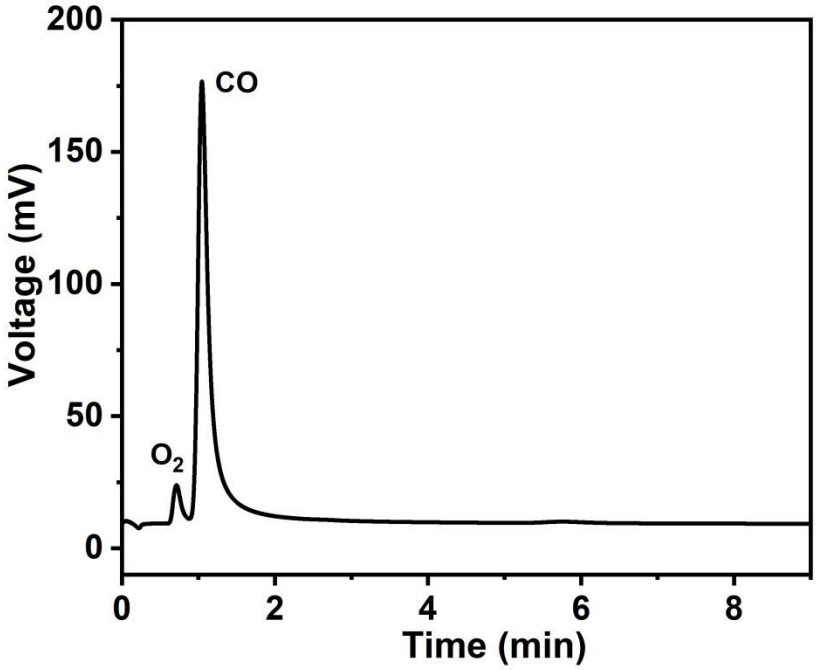

Fig. S37. GC spectra of Q[8]/Pt film-20 catalyzed photocatalytic CO to CO_2 in N_2.

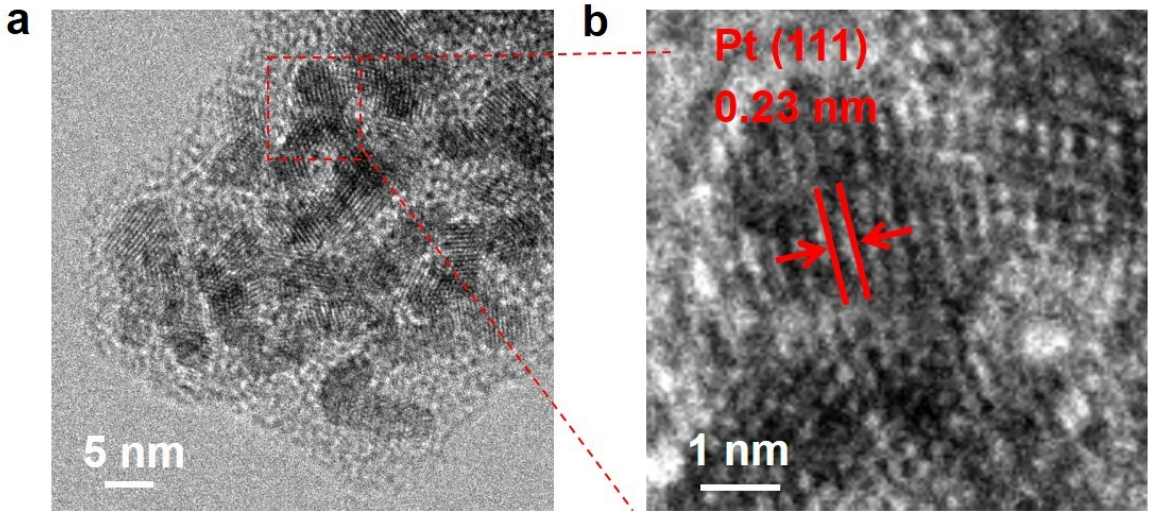

Fig. S38. (a) HR-TEM and (b) enlarged HR-TEM images of Pt nanoparticles after the photocatalytic durability test.

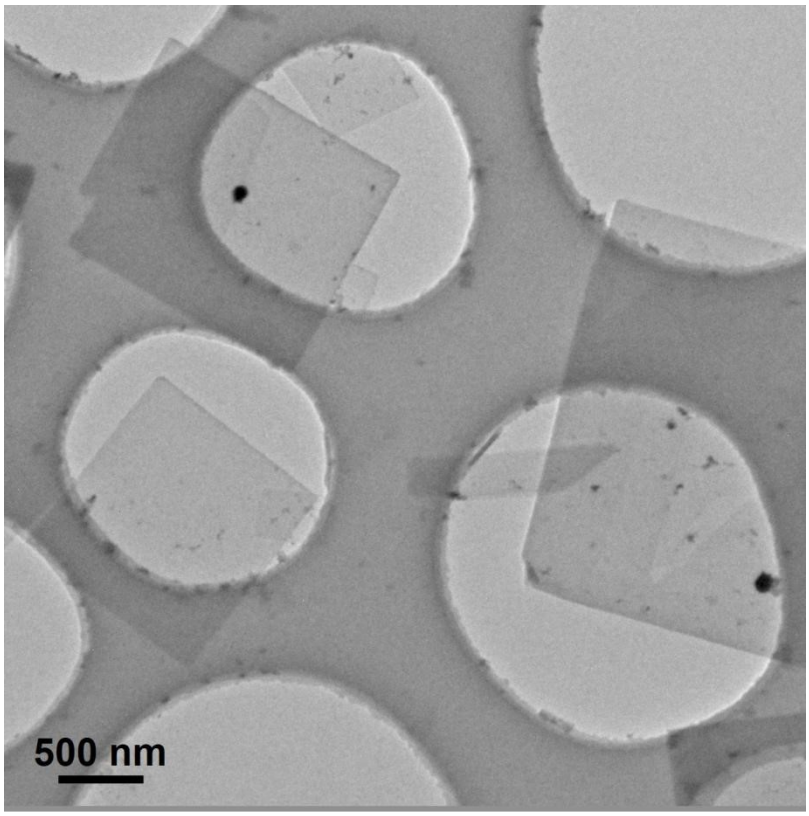

Fig. S39. TEM image of Q[8]/Pt NSs after the photocatalytic durability test.

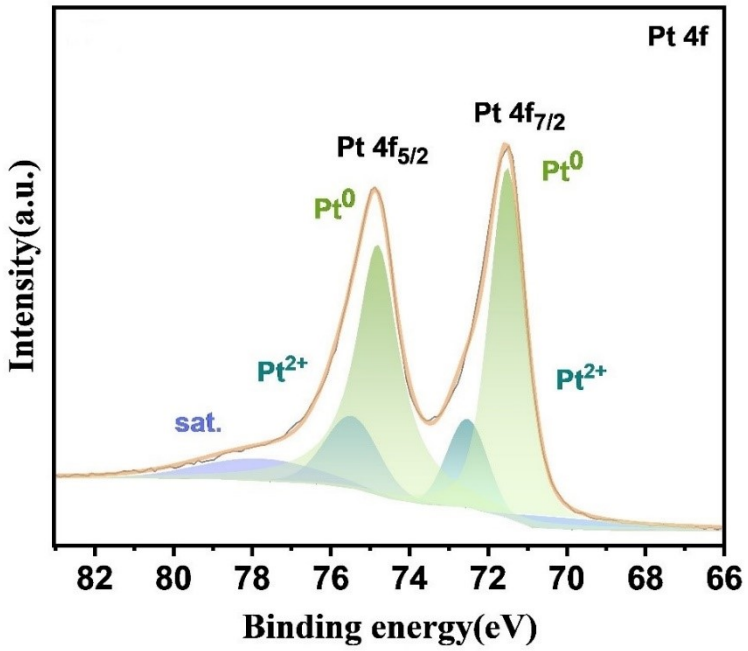

Fig. S40. The Pt 4f high-resolution spectrum of Q[8]/Pt NSs after photocatalytic durability test.

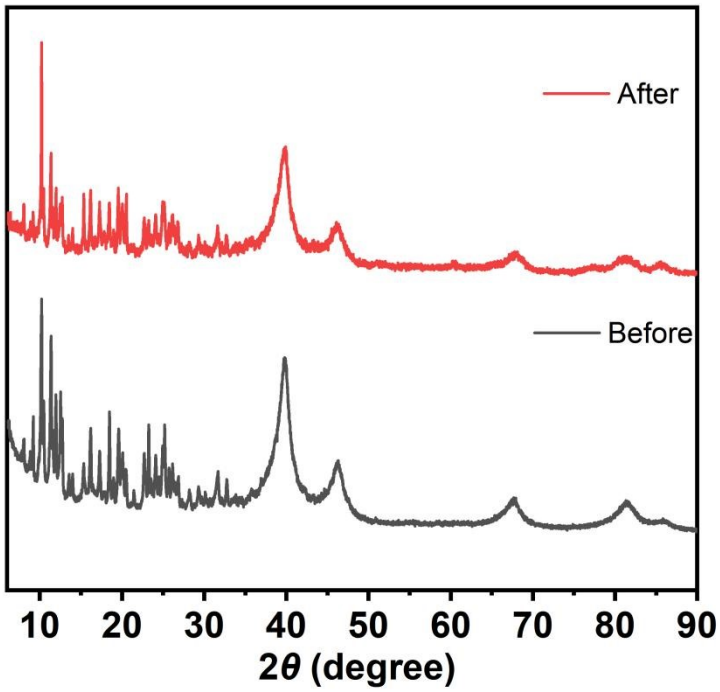

Fig. S41. PXRD patterns of Q[8]/Pt NSs powder before and after photocatalytic reactions.

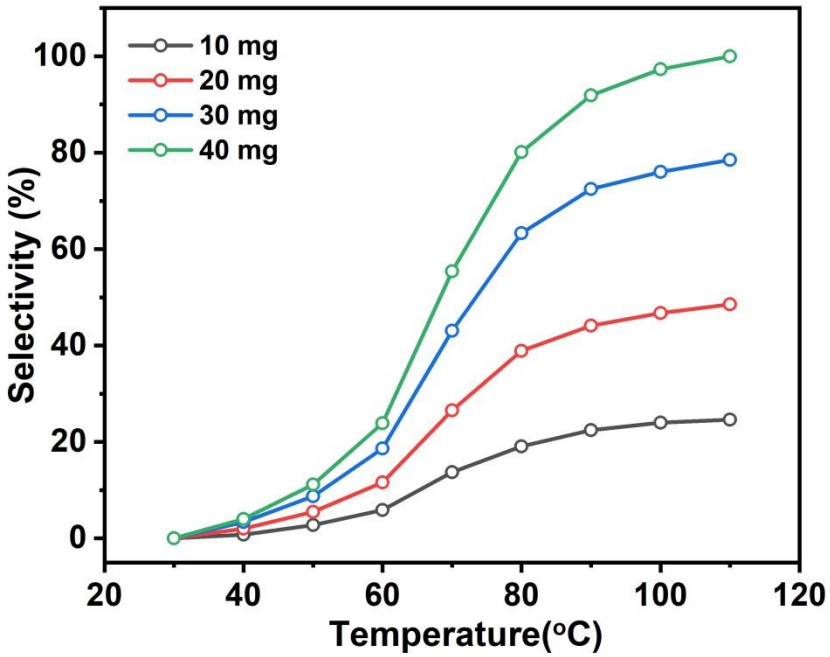

Fig. S42. Thermocatalytic CO oxidation activities of Q[8]/Pt NSs film-10/20/30/40 at 30-110 °C in an idealized gas mixture (0.8% CO, 20% O_2, He balance).

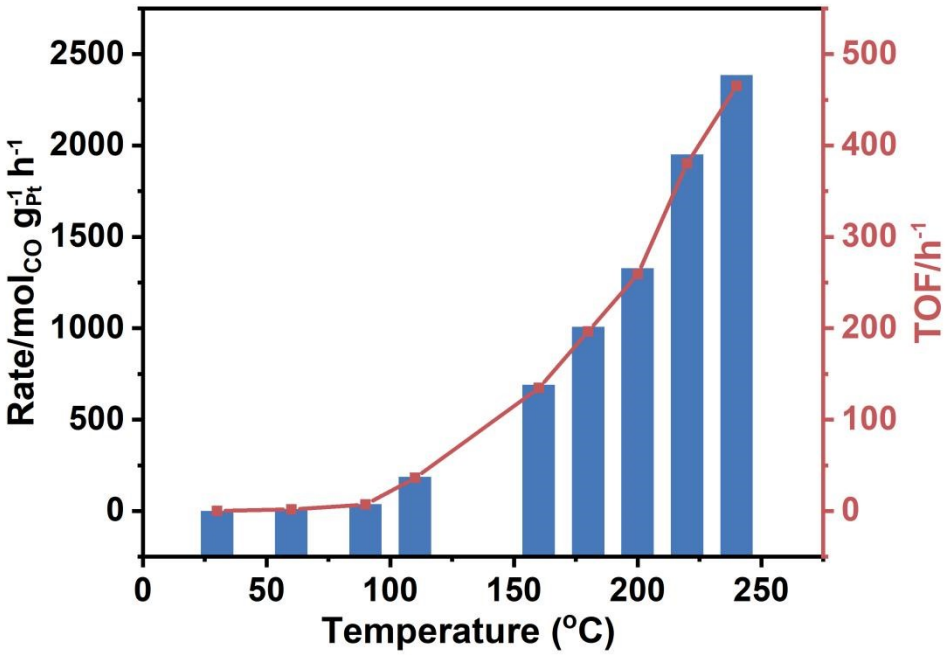

Fig. S43. Temperature dependence of the reaction rates and TOFs for thremocatalytic CO oxidation by CH_3OH-reduced Q[8]/Pt film-40 in an idealized gas mixture (0.8% CO, 20% O_2,and He balance).

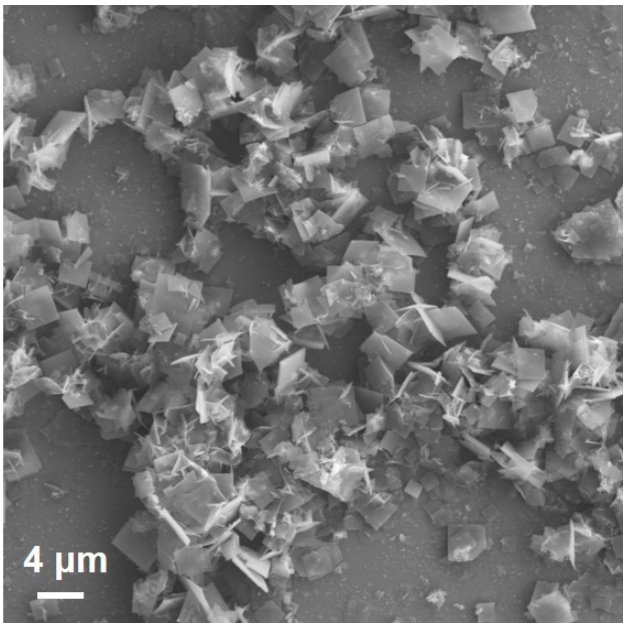

Fig. S44. SEM image of Q[8]/Pt NSs after the thremocatalytic CO oxidation durability test.

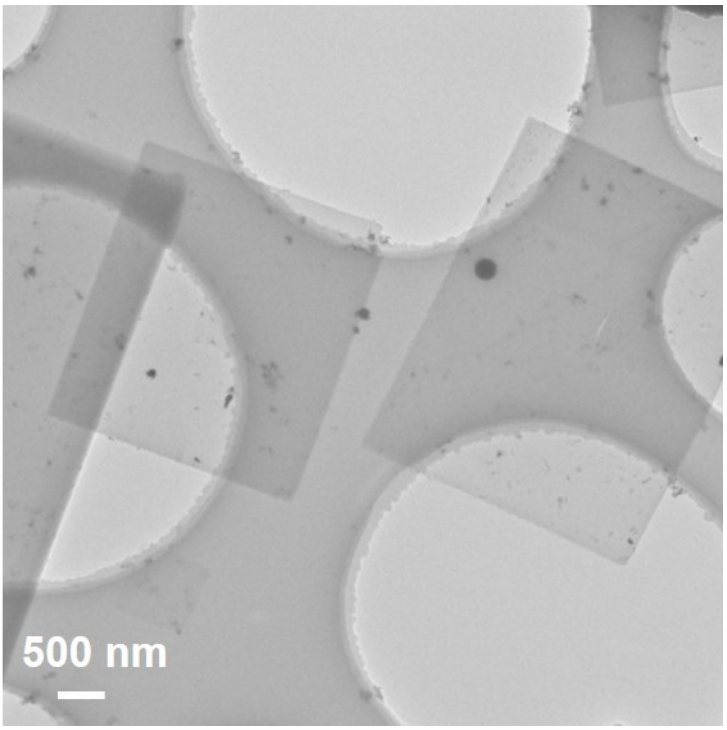

Fig. S45. TEM image of Q[8]/Pt NSs after the thremocatalytic CO oxidation durability test.

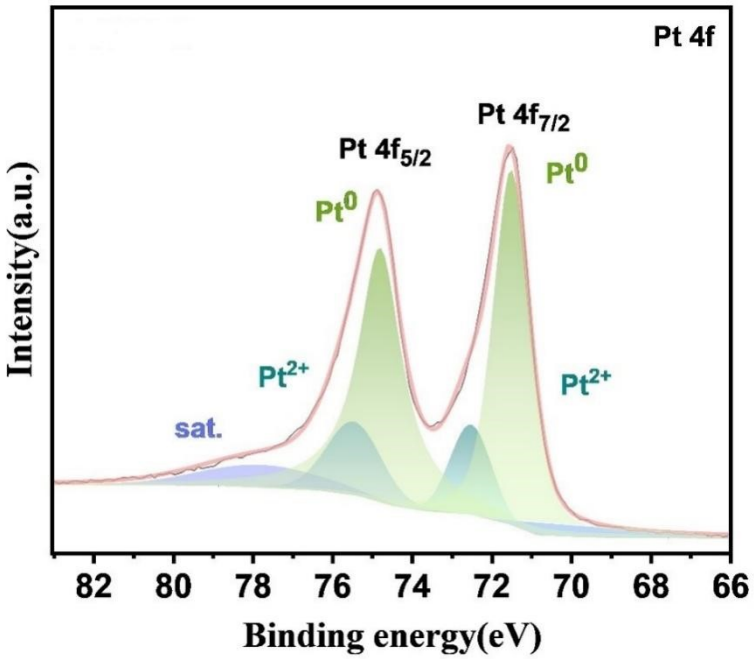

Fig. S46. The Pt 4f high-resolution spectrum of Q[8]/Pt NSs after thremocatalytic CO oxidation durability test.

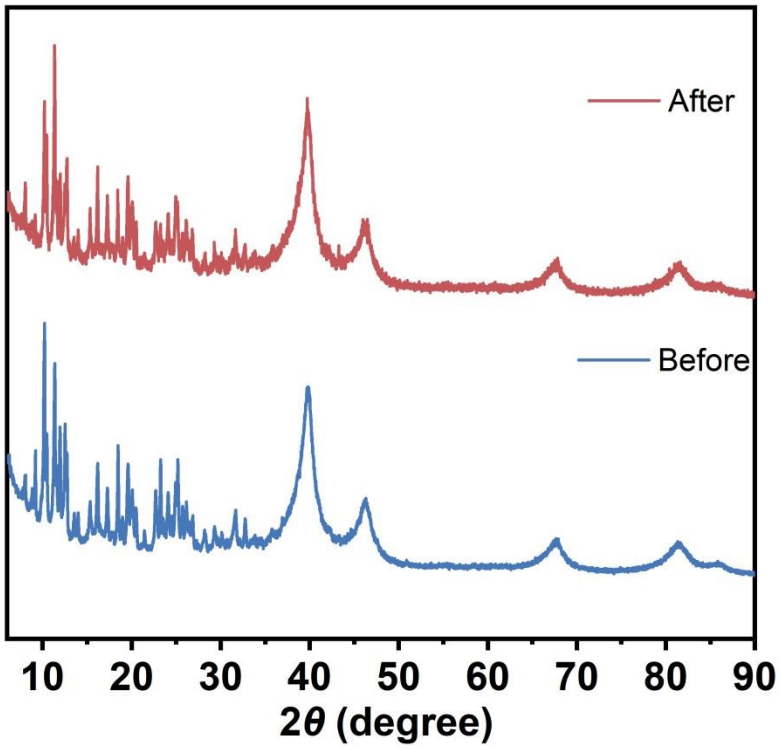

Fig. S47. PXRD patterns of Q[8]/Pt NSs film powder before and after photocatalytic reactions.

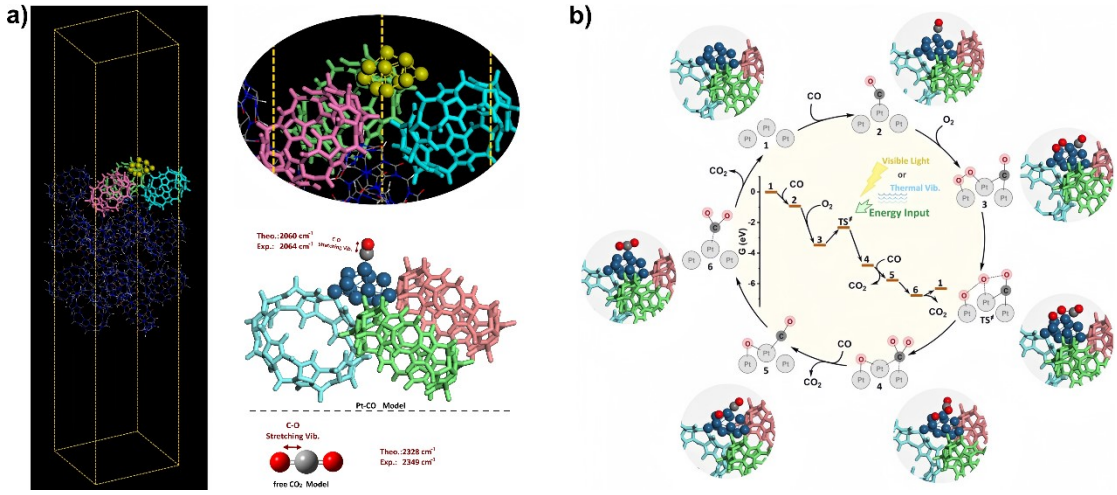

Fig. S48. (a) Simulated C-O stretching vibration in the Pt-CO model and free CO_2 molecule; (b) The catalytic mechanism of CO→CO_2 on Q[8]/Pt NSs.

Table S1. Comparison of photocatalytic activity for CO oxidation of Q[8]/Pt NSs films with other photocatalysts.

Catalyst	CO concn (ppm)	Catalyst dosage	Irradiation time (min)	Photo activity(%)	TOF (h^{-1})	Stability (time/ Percentage decline)	Ref.
Q[8]/Pt NSs film-10	8000	14.5 cm^2 thin film (10 mg)	190	100	132	-	This work
Q[8]/Pt NSs film-20	8000	14.5 cm^2 thin film (20 mg)	100	100	145	40min/2.6%	This work
Q[8]/Pt NSs film-30	8000	14.5 cm^2 thin film (30 mg)	90	100	139	-	This work
Q[8]/Pt NSs film-40	8000	14.5 cm^2 thin film (40 mg)	80	100	126	-	This work
CH_3OH-reduced Q[8]/Pt film-20	8000	20 mg	-	-	6.5	-	This work
TiO_2	50	50 cm^2 thin film	120	16	-	-	*(7)*
TiO_2/FGO	50	50 cm^2 thin film	120	51	-	-	*(7)*
TiO_2/RGO/IL-	50	50 cm^2	120	97	-	-	*(8)*

Cr		thin film					
Pd/Pt/rutile	4000	0.44	4320	100	-	35min/5%	*(9)*
MO-CN/TiP	1000	0.1 g	60	87	-	10h/10%	*(10)*

Table S2. Comparison of thremocatalytic activity for CO oxidation of Q[8]/Pt NSs films with other photocatalysts.

Catalyst	React. temp. (°C)	Pt loading [wt%]	**Photo activity(%)**	**Specific rate ($mmol_{CO}$ h^{-1} g_{metal}^{-1})**	**TOF (h^{-1})**	**Stability (time/ Percentage decline)**	**Ref.**
Q[8]/Pt NSs film-10	80	4.8	19	9026	1760	-	This work
Q[8]/Pt NSs film-20	80	4.8	40	9284	1810	1000min/1.2%	This work
Q[8]/Pt NSs film-30	80	4.8	63	9437	1840	-	This work
Q[8]/Pt NSs film-40	80	4.8	79	9330	1819	-	This work
CH_3OH-reduced Q[8]/Pt film-20	80	10.6	0	0	0	-	This work
0.5%Pt-CeO_2	60	0.5	-	1070	-	-	*(7)*
5%Pt-CeO_2	30	5	-	576	-		*(11)*
0.27%Pt-CeO_2	150	0.27	100	11100	-		*(12)*
1.0%Pt-CeO_2	100	0.5	100	500	-	300h/5.0%	*(13)*
Pt1/FeO_x	27	0.17	-	435	489.6	-	*(14)*
Pt1/FeO_x	80	0.17	100	992	1119.6	1000min/6.5%	*(14)*
Pt-SA/A-Fe_2O_3	70	1.2	100	1250	247.32	30h7.2%	*(15)*

References

1. Ji N-N*, et al.* Hexachloroplatinate(IV) Anion Induced Cucurbituril Supramolecular Assembly with Linear Channels. *Eur. J. Inorg. Chem.* **2014**, 1435-1438.
2. Chen L-X*, et al.* Outer surface interactions to drive cucurbit[8]uril-based supramolecular frameworks: possible application in gold recovery. *Chem. Commun.* **2019**, *55*, 14271-14274.
3. Delley B. From molecules to solids with the DMol3 approach. *J. Chem. Phys.* **2000**, *113*, 7756-7764.
4. Nørskov JK*, et al.* Origin of the Overpotential for Oxygen Reduction at a Fuel-Cell Cathode. *The Journal of Physical Chemistry B,* **2004***, 108*, 17886-17892.
5. Electrocatalysis: theory and experiment at the interface. *J. Phys. Chem. B,* **2008***, 10*, 3607-3608.
6. Perdew JP, Burke K, Ernzerhof M. Generalized Gradient Approximation Made Simple. *Phys. Rev. Lett.* **1996***, 77*, 3865-3868.
7. Giannakopoulou T*, et al.* Tailoring the energy band gap and edges' potentials of g-C_3N_4/TiO_2 composite photocatalysts for NOx removal. *Chem. Eng. J.* **2017**, *310*, 571-580.
8. Li T, Zhang G, Lan H, Liu H, Qu J. Enhanced Photoreduction of Chromium(VI) Intercalated Ion Exchange in $BiOBr_{0.75}I_{0.25}$ Layers Structure by Bulk Charge Transfer. *ACS Sustain. Chem. Eng.* **2019**, *7*, 2429-2436.
9. Li H, Shang H, Cao X, Yang Z, Ai Z, Zhang L. Oxygen Vacancies Mediated Complete Visible Light NO Oxidation via Side-On Bridging Superoxide Radicals. *Environ.Sci. Technol.* **2018***, 52*, 8659-8665.
10. Zhang X*, et al.* Porous two-dimension MnO_2-C_3N_4/titanium phosphate nanocomposites as efficient photocatalsyts for CO oxidation and mechanisms. *Appl. Catal., B* **2021**, *282*, 119563.
11. Meunier FC*, et al.* Synergy between Metallic and Oxidized Pt Sites Unravelled during Room Temperature CO Oxidation on Pt/Ceria. *Angew. Chem. Int. Ed.* **2021**, *60*, 3799-3805.
12. Wang H*, et al.* Surpassing the single-atom catalytic activity limit through paired Pt-O-Pt ensemble built from isolated Pt1 atoms. *Nat. Commun.* **2019***, 10*, 3808.
13. Nie L*, et al.* Activation of surface lattice oxygen in single-atom Pt/CeO_2 for low-temperature CO oxidation. *Science* **2017**, *358*, 1419-1423.
14. Qiao B*, et al.* Single-atom catalysis of CO oxidation using Pt1/FeOx. *Nat. Chem.* **2011**, *3*, 634-641.
15. Chen W*, et al.* Strong Electronic Interaction of Amorphous Fe_2O_3 Nanosheets with Single-Atom Pt toward Enhanced Carbon Monoxide Oxidation. *Adv. Funct. Mater.* **2019**, *29*, 1904278.